

A weakly nonlinear framework to study shock–vorticity interaction

Pranav Thakare¹, Vineeth Nair^{1,†} and Krishnendu Sinha^{1,†}

¹Department of Aerospace Engineering, Indian Institute of Technology Bombay

(Received 8 June 2021; revised 27 September 2021; accepted 27 November 2021)

Linear interaction analysis (LIA) is routinely used to study the shock–turbulence interaction in supersonic and hypersonic flows. It is based on the inviscid interaction of elementary Kovásznyai modes with a shock discontinuity. LIA neglects nonlinear effects, and hence it is limited to small-amplitude disturbances. In this work, we extend the LIA framework to study the fundamental interaction of a two-dimensional vorticity wave with a normal shock. The predictions from a weakly nonlinear framework are compared with high-order accurate numerical simulations over a range of wave amplitudes (ϵ), incidence angles (α) and shock-upstream Mach numbers (M_1). It is found that the nonlinear generation of vorticity at the shock has a significant contribution from the intermodal interaction between vorticity and acoustic waves. Vorticity generation is also strongly influenced by the curvature of the normal shock wave, especially for high incidence angles. Further, the weakly nonlinear analysis is able to predict the correct scaling of the nonlinear effects observed in the numerical simulations. The analysis also predicts a Mach number dependent limit for the validity of LIA in terms of the maximum possible amplitude of the upstream vorticity wave.

Key words: compressible turbulence, shock waves, supersonic flow

1. Introduction

The interaction of a shock wave with turbulence is a problem of fundamental interest, as well as practical relevance in high-speed flows. Turbulence affects the structure of the shock and, in return, shock significantly amplifies the turbulent fluctuations passing through it (Andreopoulos, Agui & Briassulis 2000). Shock–turbulence interaction has various applications in critical engineering problems such as scramjet propulsion (Liu, Sheng & Sisljan 1995; Livescu & Ryu 2016), inertial confinement fusion (Lele & Larsson 2009; Livescu & Ryu 2016) and cosmic events like supernovae explosions (Ranjan, Oakley & Bonazza 2011). A lot of scientific effort has been spent to understand the physics of

† Email addresses for correspondence: vineeth@aero.iitb.ac.in, krish@aero.iitb.ac.in

the problem and to predict the post-shock turbulence field accurately. The majority of the research is theoretical (Mahesh *et al.* 1995; Wouchuk, de Lira & Velikovich 2009; Huete Ruiz de Lira, Velikovich & Wouchuk 2011; Donzis 2012*a,b*; Huete Ruiz de Lira, Wouchuk & Velikovich 2012; Quadros, Sinha & Larsson 2016*b*; Chen & Donzis 2019) and computational (Lee, Lele & Moin 1993; Mahesh, Moin & Lele 1996; Larsson & Lele 2009; Larsson, Bermejo-Moreno & Lele 2013; Ryu & Livescu 2014; Chen & Donzis 2019), while a limited number of experimental studies (Barre, Alem & Bonnet 1996; Auvity, Barre & Bonnet 2002) have also been reported.

Small fluctuations in compressible turbulence can be represented using three fundamental modes (Kovácsznay 1953): vorticity, entropy and acoustics. A theoretical method that uses this decomposition to study the interaction of homogeneous isotropic turbulence with a normal shock wave is known as linear interaction analysis (LIA) (Moore 1954; Ribner 1954). LIA is linear and inviscid and uses concepts from wave physics to study the interaction between flow disturbances in one or more fundamental modes and a normal shock. The analysis assumes that the shock wave is a gas-dynamic discontinuity in the flow. LIA also relies on the assumption that the interaction time scales are small compared with the time scales of the turbulent fluctuations.

Interaction of a single vorticity wave with a shock is an elementary problem routinely used to understand the broader features of the shock–turbulence interaction. Disturbances in vorticity, with some orientation to the free stream on interacting with the shock, produce wave disturbances in all three modes, which can be analysed independently. Inter-modal interactions are not considered in LIA. The amplitudes of the modal disturbances downstream of the shock are evaluated using Rankine–Hugoniot (R-H) equations. Superposition of the modal disturbances downstream of the shock manifests the required flow fluctuations approximately for low amplitudes of the upstream vorticity wave.

Moore (1954) and Ribner (1954) independently laid the basis for LIA several decades ago. Using Kovácsznay mode decomposition (Kovácsznay 1953), Moore (1954) studied the unsteady interaction of an acoustic wave with a normal shock and Ribner (1954) investigated the interaction of a vorticity wave with a normal shock. Chang (1957) extended LIA by supplementing the necessary expressions for the case of interaction of entropy disturbances with a normal shock. McKenzie & Westphal (1968) later implemented LIA theory to investigate the effect of small amplitude fluctuations in the flow interacting with an oblique shock.

In recent times, LIA has been used extensively to investigate the physical mechanisms responsible for turbulence amplification by shocks. Mahesh *et al.* (1996) analysed the interaction of disturbances in vorticity and entropy with a normal shock, where they considered the effect of upstream entropy fluctuations on the post-shock flow-field. Subsequently, Fabre, Jacquin & Sesterhenn (2001) analysed the interaction of an entropy spot with a normal shock using LIA, where elementary waves of entropy fluctuations were used to construct the entropy spot. A similar approach was followed by Griffond (2005) to study the effect of a mixture of gases (represented as elementary waves of fluctuating concentration) interacting with a normal shock. Recently, Quadros *et al.* (2016*b*) investigated the turbulent energy flux generated by a normal shock and Farag, Boivin & Sagaut (2019) studied the interaction of entropy spots with heat absorbing/releasing shock waves using LIA.

Numerical simulations provide a complementary approach to study the shock–turbulence interaction. Zang, Hussaini & Bushnell (1984) computed the solutions for planar waves of each of the fundamental Kovácsznay modes interacting with normal shocks of

varying strengths. Their analysis was restricted to incident waves making an angle of 30° with the shock-normal direction. Mahesh *et al.* (1996) investigated individual interaction of acoustic and vorticity–entropy waves with a normal shock using direct numerical simulation (DNS). Results for turbulent kinetic energy (TKE) and vorticity variances from computations matched qualitatively with results from LIA. Recently, the works of Sethuraman, Sinha & Larsson (2018), Tian *et al.* (2017), Quadros, Sinha & Larsson (2016a), Quadros *et al.* (2016b), Livescu & Ryu (2016), Ryu & Livescu (2014), Larsson *et al.* (2013) and Larsson & Lele (2009) have computed the post-shock statistics of various second-moments for a range of shock Mach numbers. Results obtained from DNS are compared with LIA and a good match is found for cases with relatively low amplitude turbulent fluctuations upstream of the shock.

It is generally accepted that LIA predictions are valid in the limit of vanishing turbulent Mach number and infinite Reynolds number. Here, turbulent Mach number is given by $M_t = \sqrt{2k}/\bar{a}$, k is the turbulent kinetic energy and \bar{a} is the mean speed of sound. Many of the comparisons of LIA and DNS, either for varying M_t (Ryu & Livescu 2014) or by artificially removing viscous dissipation (Larsson *et al.* 2013), show this qualitative trend. However, very few quantitative estimates exist for the bounds of validity of LIA. The question as to within what range of governing parameters the results from LIA can be considered reliable is still open (Chen & Donzis 2019). This question has become particularly relevant in recent times, where LIA is being used as a surrogate to numerical simulations in regions of shock waves (Braun, Pullin & Meiron 2019) and LIA-based turbulence models are increasingly being used in practical applications (Sinha, Mahesh & Candler 2005; Pasha & Sinha 2012; Roy, Pathak & Sinha 2018; Vemula & Sinha 2020).

Lee *et al.* (1993) studied the interaction of isotropic quasi-incompressible turbulence with a weak shock wave using DNS for $1.05 \leq M_1 \leq 1.2$. They found that the results from LIA compare well with the DNS solution for the condition $M_t^2 < 0.1(M_1^2 - 1)$. They asserted that inside the stated limit, the amplification mechanism for turbulent kinetic energy and vorticity is linear. The specified limit is valid for weak shock waves only. Similarly, Ryu & Livescu (2014) proved that the LIA solution for shock–turbulence interaction converges to DNS as M_t tends to smaller values. This work shows the reliability of LIA for problems involving a notable separation between turbulence scales (η) and shock width (δ), i.e. for small $\delta/\eta \simeq 7.69M_t/Re_\lambda^{0.5}(M_1 - 1)$, which is a criteria for scale separation first given by Donzis (2012a). Here, Re_λ represents Taylor Reynolds number and M_1 is the shock Mach number. At fixed Re_λ and M_1 , the convergence of LIA to DNS is governed by $M_t \rightarrow 0$. At higher M_t , the amplification of Reynolds stresses and vorticity is found to significantly deviate from LIA predictions, which shows the importance of nonlinear effects.

Chen & Donzis (2019) discussed a universal scaling parameter K for the amplification factor of streamwise velocity, which leads to the criteria for the viability of LIA. It involves the combined effect of M_t , upstream Mach number M_1 and an account of the viscous effects through the Reynolds number. The scaling parameter K is defined as $K = \delta_l/\eta$, where δ_l is the shock thickness and η represents the Kolmogorov length scale. For low values of K , results approach the limits specified by LIA; i.e. the amplification factor becomes a function of M_1 only. Furthermore, Grube & Martín (2021) studied the redistribution of energy between the transverse and streamwise Reynolds stresses in the shock–turbulence interaction using LIA and DNS. They developed a model for nonlinear interactions using LIA and the eddy viscosity approximation to quantify the redistribution of energy between transverse and streamwise Reynolds stresses.

The objective of the current work is to address the open questions concerning LIA by analysing the elementary interaction of a vorticity wave with a normal shock both numerically and theoretically. Vorticity fluctuations are fundamental to turbulence, and they constitute one of the fundamental modes in compressible turbulence (Kovásznay 1953). Understanding the dynamics and evolution of vorticity fluctuations is crucial in high-speed applications, for instance, in studying turbulent mixing at supersonic Mach numbers in scramjet combustors, in the description of the interaction of vortex/entropy spots with normal shocks (Ribner 1987; Fabre *et al.* 2001), bubble–shock interactions and related Richtmyer–Meshkov (R–M) instability problems (Ranjan *et al.* 2011). Further, vorticity is inherently related to enstrophy, which signifies the rate of dissipation of the turbulent kinetic energy (Sinha 2012).

We present a weakly nonlinear framework (WNLF) for the shock–vorticity interaction and study the amplification of vorticity fluctuations across the shock wave. The analysis is an extension of the LIA framework, where we retain the second-order terms in the R-H equations across the shock wave. These terms are evaluated using the LIA solution to estimate their magnitude relative to the linear effects at the shock wave. We identify the dominant nonlinear physical mechanisms that are responsible for vorticity amplification across the shock and study their variation with the amplitude and incidence angle of the vorticity wave and the strength of the shock wave. Of particular interest are the interactions between the different Kovásznyai modes and the higher-order effects of the unsteady oscillating shock wave that are neglected by the linear analysis.

The weakly nonlinear framework is validated using numerical simulations of the shock–vorticity wave interaction with the high-order accurate numerical method (Larsson & Lele 2009; Johnsen *et al.* 2010). We study the deviation of the numerical results from the LIA solution for different values of the parameters listed above. The deviation is compared with the second-order vorticity amplitude predicted by WNLF. The analytical results are found to match well with the numerical data. WNLF also predicts the correct scaling of the nonlinear effects obtained from the numerical simulations. In general, other physical mechanisms in addition to the shock-induced nonlinearities could also result in nonlinear effects in vorticity. This paper focuses on studying the nonlinear interactions at the shock wave and especially strives to isolate the nonlinear effects arising from shock-induced nonlinear modal interactions. Viscous effects are assumed to be negligible in the vicinity of the shock. Both the numerical simulations and WNLF are based on the inviscid and ideal gas framework. WNLF assumes the shock to be a discontinuity, while the numerical simulations capture the shock over a few grid points. Therefore, a comparison between analytical results and the numerical solution is made very close to the numerically captured shock wave.

Finally, we use WNLF to arrive at a quantitative limit for the validity of LIA. We identify the maximum amplitude of the upstream vorticity wave, for which the nonlinear amplification of vorticity is small compared with the LIA predictions. This range is found to be a function of the shock Mach number and the incidence angle of the vorticity wave. The maximum vorticity amplitude has a non-monotonic variation with shock Mach number, with different scaling for weak and strong shock waves. The variation, as expected, depends on the dominant physical mechanisms in each case. WNLF also indicates that the LIA limit can be different for different turbulence quantities (vorticity, pressure variance, Reynolds stress, etc.). This provides a possible reason why there is no universal criteria for the validity of LIA reported in the literature.

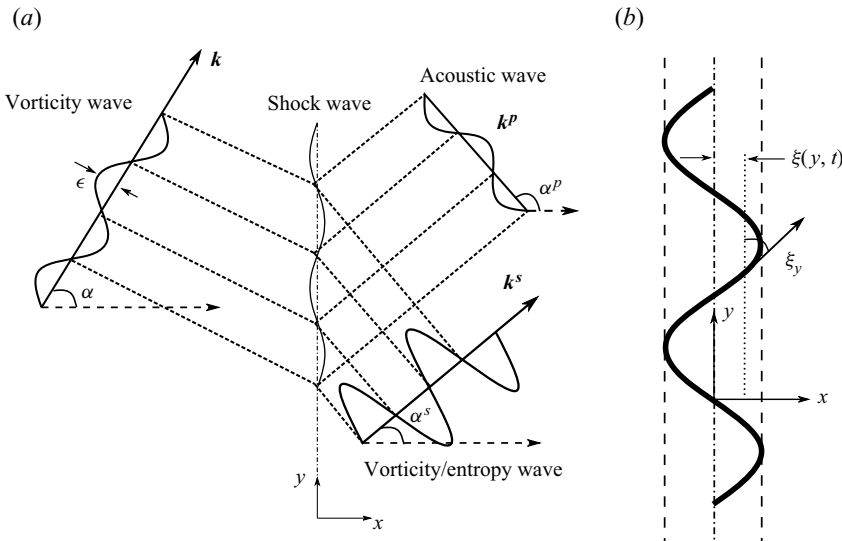


Figure 1. Schematic of the vorticity wave–normal shock interaction showing (a) the generation of acoustic and entropy waves downstream of the shock and (b) a magnified view of the shock deformation.

2. Methodology

2.1. Linear interaction analysis

Let us consider a two-dimensional, small amplitude planar vorticity wave with its wavenumber vector k inclined at an angle α with the x -axis (see figure 1). Mathematically, the vorticity wave can be represented as

$$\frac{\Omega'}{k\bar{U}_1} = -i\epsilon \exp(i(\mathbf{k} \cdot \mathbf{r} - \omega t)), \quad (2.1)$$

where \mathbf{r} is the position vector, k is the magnitude of the wavenumber vector and ω denotes the angular frequency of the vorticity wave. The quantity ϵ is the amplitude of the vorticity wave normalized by the wavenumber and mean velocity \bar{U}_1 . The vorticity wave is advected by a one-dimensional, uniform mean flow of velocity towards the normal shock initially located along the y -axis. The shock deforms in response to the fluctuations and the local position of the unsteady shock is given by the function $\xi(y, t)$. The derivative ξ_y thus represents the angular deformation of the shock (see figure 1).

Small amplitude vorticity fluctuations are solenoidal fluctuations that impose a divergence-free condition on the fluctuating velocity field. The velocity fluctuations upstream of the shock (subscript 1) are given as

$$\frac{u'_1}{\bar{U}_1} = \epsilon \sin \alpha \exp(ik(x \cos \alpha + y \sin \alpha) - i\omega t), \quad (2.2)$$

$$\frac{v'_1}{\bar{U}_1} = -\epsilon \cos \alpha \exp(ik(x \cos \alpha + y \sin \alpha) - i\omega t), \quad (2.3)$$

where u' and v' represent the velocity fluctuations in the shock normal (x) and shock parallel (y) directions, respectively. Substituting the above forms in the linearized momentum equation shows that vorticity waves do not produce pressure fluctuations in the linear, inviscid limit. Physically, because vorticity fluctuations travel with the mean

flow, they do not require pressure fluctuations to advect. Also, thermodynamics dictates that the vorticity wave does not create any fluctuations in entropy in the linear limit.

We investigate the interaction of such vorticity fluctuations with a normal shock and obtain the perturbation field downstream using LIA. We follow the works of Fabre *et al.* (2001), Mahesh *et al.* (1996), Moore (1954) and Kovásznyai (1953), and the reader may refer to these for additional details on the theory. We perform this investigation for a constant specific heat ratio of air $\gamma = 1.4$.

The incident vorticity wave refracts whereas acoustic and entropy waves are generated at the shock, with inclinations α^p and α^s , respectively. The refracted vorticity wave has the same inclination as that of the downstream entropy wave. Let the wavenumber of the downstream acoustic and non-acoustic waves (vorticity and entropy) be k^p and k^s , respectively. The post-shock acoustic wave can be either propagating or decaying depending on the angle of the incident wave. There exists a critical angle, α_c for $\alpha \in [0, \pi/2]$, beyond which the acoustic waves decay immediately behind the shock.

The linearized Euler equations with the linearized R-H conditions as the boundary conditions at the shock are solved to obtain post-shock wave characteristics. The downstream fluctuations have the same y and t dependencies as the perturbed shock front (or the incident wave) as dictated by R-H conditions. The dispersion relation at the shock constrained by the continuity equation then yields that the transverse wavenumber and the angular frequency of the wave remain invariant across the shock. Thus, we get

$$\cot \alpha^s = r \cot \alpha, \tag{2.4}$$

where r is the mean velocity ratio ($\bar{U}_1/\bar{U}_2 = \bar{\rho}_2/\bar{\rho}_1$) across the shock. The ratio r is an estimate of the amount by which the streamwise wavenumber of the vorticity wave gets compressed. The wavenumber for the acoustic wave k^p is then determined from the acoustic wave equation; details are given by Mahesh *et al.* (1995).

The disturbance field downstream of the shock (subscript 2) can be written in terms of the vorticity fluctuations Ω'_2 , entropy fluctuations s'_2 and pressure fluctuations p'_2 as

$$\frac{\Omega'_2}{k^s \bar{U}_2} = -i \epsilon Z_{vv} \exp(ik^s(x \cos \alpha^s + y \sin \alpha^s) - i\omega t), \tag{2.5}$$

$$\frac{s'_2}{c_p} = \epsilon Z_{vs} \exp(ik^s(x \cos \alpha^s + y \sin \alpha^s) - i\omega t), \tag{2.6}$$

$$\frac{p'_2}{\bar{P}_2} = \epsilon Z_{vp} \exp(ik^p(x \cos \alpha^p - \eta x + y \sin \alpha^p) - i\omega t), \tag{2.7}$$

where Z_{vv} , Z_{vs} , Z_{vp} are the corresponding transfer coefficients and are functions of α and M_1 . The quantities c_p , \bar{P}_2 and η represent the specific heat of fluid, mean pressure downstream of the shock and decay parameter of acoustic wave amplitude normal to the shock, respectively. Under the assumptions of LIA, decay of pressure perturbations at the shock ($\eta \neq 0$) occurs when α exceeds α_c .

Both vorticity and acoustic modes of fluctuations generate velocity fluctuations downstream of the shock wave independent of each other in the linear limit. Accordingly, shock normal (u'_2) and shock parallel (v'_2) velocity fluctuations downstream can be

written as

$$\frac{u'_2}{\bar{U}_2} = \epsilon \sin \alpha^s Z_{vv} \exp(ik^s(x \cos \alpha^s + y \sin \alpha^s) - i\omega t) + \left\{ \frac{\cos \alpha^p + i\eta}{\gamma M_2 \zeta} \right\} \frac{p'_2}{\bar{P}_2}, \quad (2.8)$$

$$\frac{v'_2}{\bar{U}_2} = -\epsilon \cos \alpha^s Z_{vx} \exp(ik^s(x \cos \alpha^s + y \sin \alpha^s) - i\omega t) + \left\{ \frac{\sin \alpha^p}{\gamma M_2 \zeta} \right\} \frac{p'_2}{\bar{P}_2}, \quad (2.9)$$

where ζ is a function of the decaying parameter (η). The first and second terms on the right-hand side of (2.8) and 2.9 represent the contribution from vorticity mode and acoustic mode, respectively.

Corrugation of the shock measured with respect to its mean position is given as

$$k\xi = \epsilon Z_{vx} \exp(iky \sin \alpha - i\omega t), \quad (2.10)$$

where Z_{vx} is the transfer coefficient for shock perturbation. Differentiating with respect to time gives the instantaneous shock corrugation speed in the streamwise direction:

$$\frac{\xi_t}{\bar{U}_1} = -i\epsilon \cos \alpha Z_{vx} \exp(iky \sin \alpha - i\omega t). \quad (2.11)$$

Substituting these expressions in the linearized Euler equations allows the estimation of the transfer coefficients of the disturbance (Z_{vv} , Z_{vx} , Z_{vp} and Z_{vs}) for the post-shock regime. Mathematically, these transfer coefficients are computed as

$$A \begin{pmatrix} Z_{vv} \\ Z_{vs} \\ Z_{vp} \\ Z_{vx} \end{pmatrix} = \begin{pmatrix} -1 \\ -r \\ 0 \\ r^2 \\ \hline (\gamma - 1)M_1^2 \end{pmatrix}, \quad (2.12)$$

where

$$A = \begin{pmatrix} \sin \alpha^s & -1 & \frac{1}{\gamma} + \frac{\cos \alpha^p + i\eta}{\gamma M_2 \zeta} & i(r - 1)\cos \alpha^p \\ 2\sin \alpha^s & -1 & \frac{M_2^2 + 1}{\gamma M_2^2} + \frac{\cos \alpha^p + i\eta}{\gamma M_2 \zeta} & 0 \\ -\cos \alpha^s & 0 & \frac{\sin \alpha^p}{\gamma M_2 \zeta} & i(1 - r)\sin \alpha \\ \sin \alpha^s & \frac{1}{(\gamma - 1)M_2^2} & \frac{1}{\gamma M_2^2} + \frac{\cos \alpha^p + i\eta}{\gamma M_2 \zeta} & ir(r - 1)\cos \alpha^p \end{pmatrix}. \quad (2.13)$$

Figure 2(a) shows the variation of the transfer coefficients with α for a fixed M_1 . The transfer coefficients for vorticity Z_{vv} and shock deformation Z_{vx} show a monotonic increase with α in the propagating regime ($\alpha < \alpha_c$), reaching a maximum at α_c . They decrease with further increase of α in the decaying regime. Transfer coefficients for pressure and entropy have a non-monotonic variation in the propagative regime. For all M_1 and α , LIA predicts that Z_{vv} is the largest, which indicates that the linear processes are dominated by vorticity amplification (see figures 2(a) and 2(b)). In the limit of a vanishing shock wave ($M_1 = 1$), there is no amplification of vorticity ($Z_{vv} = 1$) and Z_{vv} increases in magnitude for increases in M_1 to reach an asymptotic value as $M_1 \rightarrow \infty$.

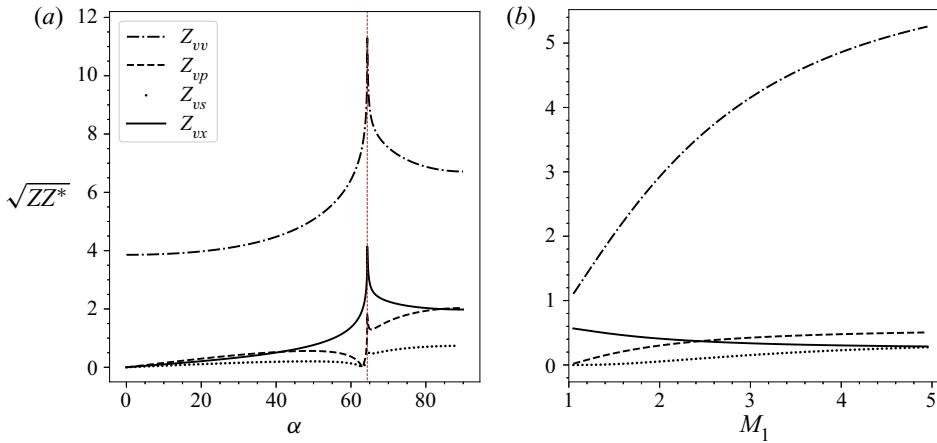


Figure 2. Variation of transfer coefficients with (a) α at $M_1 = 3$ and (b) M_1 at $\alpha = 30^\circ$. Dashed red line in panel (a) indicates α_c .

The relative magnitude of the transfer coefficients and their variation with α and M_1 play an important role in the weakly nonlinear framework (WNLf) presented subsequently. The high values of Z_{vv} and Z_{vx} in the vicinity of α_c degrade the accuracy of the numerical solution presented in the paper. Hence, we restrict our numerical simulations to low values of α in the propagating regime away from α_c .

2.2. Numerical simulations

The interaction of the vorticity wave with a normal shock is studied numerically over a two-dimensional domain, as shown in figure 3. The length of the computational domain is 4π and 2π in the streamwise (x) and transverse (y) directions, respectively. Four stations in the x -direction are marked in figure 3. We specify a supersonic boundary condition for the inflow station ($x = -\pi$), where velocity fluctuations

$$u' = \epsilon \bar{U}_1 \sin \alpha \cos(k \sin \alpha y - \omega t), \tag{2.14}$$

$$v' = -\epsilon \bar{U}_1 \cos \alpha \cos(k \sin \alpha y - \omega t), \tag{2.15}$$

are superimposed on a one-dimensional supersonic streamwise mean flow \bar{U}_1 . A non-reflecting subsonic boundary condition is applied at the outflow ($x = 3\pi$) and a periodic boundary condition is used for the transverse boundaries.

The flow downstream of the normal shock is subsonic and allows spurious acoustic waves from the outflow boundary to propagate towards the shock. These acoustic reflections are undesirable and need to be avoided or damped. A numerical sponge similar to that prescribed by Larsson & Lele (2009) and Sethuraman *et al.* (2018) is used to achieve this. In our numerical domain, a sponge is used from $x = 2\pi$ to $x = 3\pi$ and it dampens the fluctuations to a target state defined by the R-H conditions for the mean flow.

Compressible Euler equations for an ideal gas ($\gamma = 1.4$) are solved for various M_1 using the solution-adaptive finite-difference Hybrid code (Larsson & Lele 2009). A fifth-order accurate WENO scheme with Roe-flux splitting is used to calculate the approximate fluxes near the shock and a sixth-order accurate central difference scheme is used for the remainder of the domain. The system of equations is integrated in time using a fourth-order accurate, explicit Runge–Kutta (RK4) scheme. Numerical shock is identified

Weakly nonlinear framework

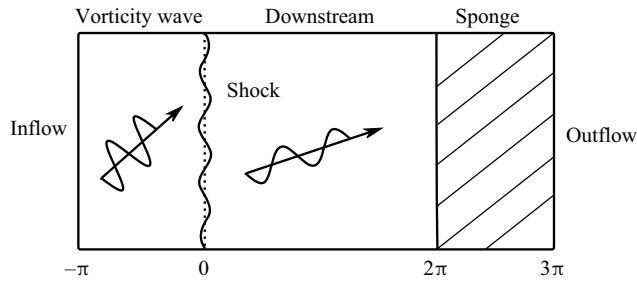


Figure 3. Numerical domain: $x = -\pi$ shows the inlet boundary; $x = 0$ is the initial position of the normal shock; $x = 2\pi$ the start of a numerical sponge; and $x = 3\pi$ the outlet boundary and end of the numerical sponge.

using a modified Ducros sensor (Larsson & Lele 2009). The shock is identified as the region where negative dilatation is greater than the low-pass filtered vorticity magnitude. This numerical procedure has been verified and validated on various problems of interest (Larsson & Lele 2009; Johnsen *et al.* 2010; Larsson *et al.* 2013), and additional details about the code can be found in Sethuraman *et al.* (2018), Bermejo-Moreno *et al.* (2013), Larsson *et al.* (2013) and Larsson & Lele (2009).

Flow variables are normalized so that the upstream velocity equals the upstream Mach number (M_1). For this purpose, we use density and sound speed upstream of the shock as characteristic variables, whereas the y -component of wavenumber (k_y) is used to normalize different length scales. Pressure is normalized using the characteristic density and sound speed, whereas vorticity is normalized using k_y and sound speed upstream of the shock. The equations are integrated in time with a Courant–Friedrichs–Lewy (CFL) number of 0.8, which corresponds to a flow time scale of ~ 0.003 . It takes approximately 200 to 300 time steps to simulate one wave passage through the shock.

Initially, the normal shock lies at $x = 0$ and oscillates in the transverse direction when fluctuations impinge on it and change the downstream pressure. Mismatch in the pressure levels downstream of the shock with that obtained from R-H conditions causes the shock to drift slowly. We use a time-dependent back-pressure controller (Larsson & Lele 2009) to reduce the shock movement and make it as stationary as possible around the desired location, $x = 0$. We follow the implementation procedure prescribed by Sethuraman *et al.* (2018) to control the movement of the shock using the back-pressure controller.

The time taken by the initial disturbances to adjust to the boundary conditions is considered as an initial transient. We track the shock movement during this time as in Sethuraman *et al.* (2018) to ascertain that the post-shock statistics are computed after the initial transients have passed. The flow statistics achieve a steady-state value at this point.

Post-shock statistics are collected at a fixed x -location by averaging over the transverse (y) direction and time. For averaging, 61 time realizations distributed uniformly over a wave period are used. Flow statistics change negligibly when the averaging time is increased to multiple wave periods from those obtained over one wave period. This signifies that the statistics evaluated over one wave period are sufficiently time-independent, and the initial transients in the numerical simulations have vanished.

Figure 4(a) shows the variation of the root-mean-squared value of fluctuation kinetic energy (FKE) downstream of the shock computed for four different grid resolutions. The data are normalized by its upstream value to obtain the amplification across the shock. We observe a systematic grid-convergence to the finest grid and the LIA solution. We also note that FKE has a wave-like variation behind the shock. This is because post-shock velocity

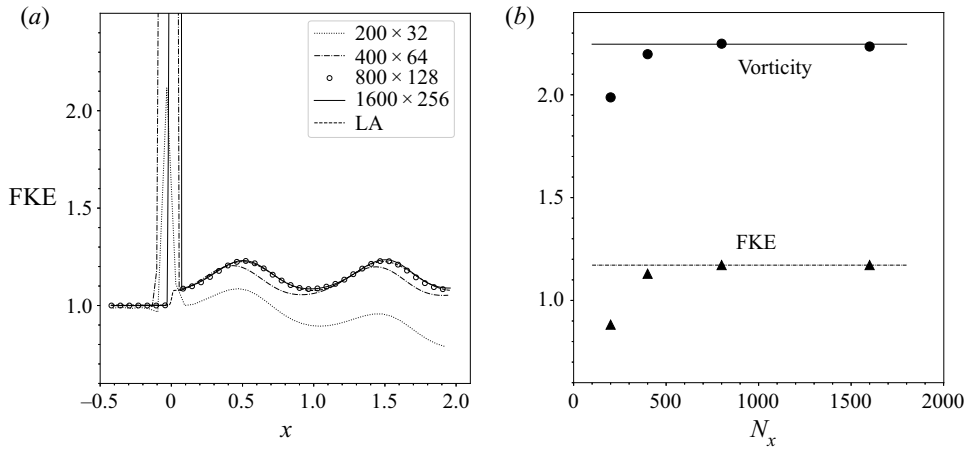


Figure 4. Effect of grid refinement on (a) the amplification of root-mean-squared fluctuation kinetic energy (FKE) and (b) the amplification of root-mean-squared value of vorticity and FKE across the shock. Here, N_x is the number of points in the streamwise direction; $M_1 = 1.75$, $\alpha = 30^\circ$ and $\epsilon = 0.1$.

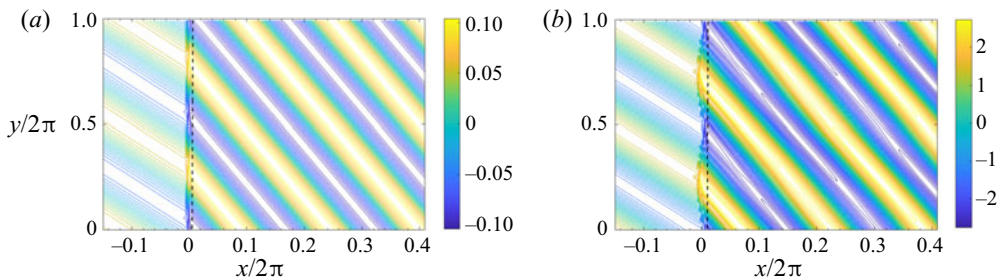


Figure 5. Vorticity contour plots at $\alpha = 30^\circ$ and $M_1 = 1.5$ for (a) $\epsilon = 0.01$ and (b) $\epsilon = 0.25$. The interaction and refraction of the vorticity wave with the shock are clearly visible. The amplitude of shock fluctuations and the nonlinearities in the downstream vorticity are larger for larger ϵ .

fluctuations have contribution both from vorticity and acoustic modes. The difference in wavenumbers of the two modes result in a periodic variation of FKE. In comparison, the upstream FKE is constant as it has contribution only from the vorticity mode.

In figure 4(b), the amplification of the root-mean-squared value of FKE and vorticity (Ω) averaged in the transverse direction and in time as well as over one wavelength of the post-shock variation is presented for four successively refined computational grids. The data show negligible change for grid sizes 800×128 and above. Therefore, we choose a grid size of 800×128 for our study and all subsequent numerical results presented are generated using this grid. The grid refinement study was performed for $M_1 = 1.75$ and $\alpha = 30^\circ$. Comparable results are obtained (not shown) for the entire range of parameters considered in this work.

Figure 5 shows the vorticity contours computed for the shock–vorticity wave interaction at $\alpha = 30^\circ$ and $M_1 = 1.5$. Two values of ϵ are used to highlight the effect of upstream vorticity amplitude. The numerical solution for $\epsilon = 0.01$ matches the vorticity pattern shown in figure 1, in terms of the refraction of the waves at the shock and the sinusoidal deformation of the shock wave. The parallel contour lines indicate two-dimensional planar waves as predicted by LIA. In comparison, the higher-amplitude interaction ($\epsilon = 0.25$)

shows deviation from the LIA solution downstream of the shock. The non-parallel vorticity contours, especially close to vorticity minima (around -2) indicate that the numerical solution is not a sinusoidal wave. The objective of this work is to study these nonlinear effects immediately downstream of the shock using the weakly nonlinear framework presented below.

3. Weakly nonlinear framework

LIA, as a theory, captures the linear effects, whereas the numerical simulations contain nonlinear effects along with linear effects. In the case of a shock–turbulence interaction, nonlinear effects become significant as ϵ increases and predictions from LIA deviate from numerical simulations for large ϵ . It has been proposed that the interaction of linear modes leads to observed higher-order effects in vorticity and other downstream fluctuation quantities (Chu & Kovásznay 1958).

To have more accurate predictions, these nonlinear effects need to be taken into account in the theory. We propose a framework which considers these effects quantitatively based on the modal interaction described by Chu & Kovásznay (1958). We call it the weakly nonlinear framework (WNLF) as the analysis uses results from LIA to study nonlinear phenomena. Therefore, we expect that its applicability is restricted to weak departures from linear behaviour. As a model problem, we apply WNLF to the shock–vorticity wave interaction problem.

Consider a one-dimensional uniform mean flow up and downstream of the shock. Integration of the momentum conservation equation along the shock normal (x) direction with the inviscid assumption gives

$$P_1 + \rho_1 U_1^2 = P_2 + \rho_2 U_2^2. \quad (3.1)$$

We decompose (3.1) into mean and fluctuating parts using classical Reynolds decomposition. Keeping terms up to second-order, we have

$$\begin{aligned} p'_1 + 2\bar{\rho}_1 \bar{U}_1 (u'_1 - \xi_t) + \rho'_1 \bar{U}_1^2 + \bar{\rho}_1 (u'_1 - \xi_t)^2 - 2\bar{\rho}_1 \bar{U}_1 v'_1 \xi_y + 2\rho'_1 \bar{U}_1 (u'_1 - \xi_t) \\ = p'_2 + 2\bar{\rho}_2 \bar{U}_2 (u'_2 - \xi_t) + \rho'_2 \bar{U}_2^2 + \bar{\rho}_2 (u'_2 - \xi_t)^2 - 2\bar{\rho}_2 \bar{U}_2 v'_2 \xi_y + 2\rho'_2 \bar{U}_2 (u'_2 - \xi_t), \end{aligned} \quad (3.2)$$

where $u' - \xi_t$ represents the streamwise velocity fluctuations relative to the unsteady shock wave and $v' \xi_y$ is the component of the transverse velocity fluctuations in the shock-normal direction.

For one-dimensional steady mean flow, the vorticity fluctuations are written in terms of the spatial gradients of velocity fluctuations, i.e.

$$\Omega' = \frac{\partial v'}{\partial x} - \frac{\partial u'}{\partial y}. \quad (3.3)$$

We proceed to derive an expression for shock-downstream vorticity fluctuations in terms of the upstream flow quantities. To this end, we differentiate (3.2) to obtain $\partial u' / \partial y$

downstream of the shock as

$$\begin{aligned} \bar{U}_2 \frac{\partial u'_2}{\partial y} &= \bar{U}_2 \frac{\partial u'_1}{\partial y} + \bar{U}_2 \frac{\partial}{\partial y} \left\{ \frac{p'_1 - p'_2}{2\bar{\rho}_1 \bar{U}_1} + \frac{\bar{U}_1 \rho'_1}{2\bar{\rho}_1} - \frac{\bar{U}_2 \rho'_2}{2\bar{\rho}_2} \right\} \\ &+ \bar{U}_2 \frac{\partial}{\partial y} \left\{ \xi_y (v'_2 - v'_1) + \frac{\rho'_1 (u'_1 - \xi_t)}{\bar{\rho}_1} - \frac{\rho'_2 (u'_2 - \xi_t)}{\bar{\rho}_2} \right\} \\ &+ \bar{U}_2 \frac{\partial}{\partial y} \left\{ \frac{(u'_1 - \xi_t)^2}{2\bar{U}_1} - \frac{(u'_2 - \xi_t)^2}{2\bar{U}_2} \right\}. \end{aligned} \tag{3.4}$$

We follow the approach of Sinha (2012) to derive a relation for the gradient $\partial v'/\partial x$. We write the momentum equation in the y -direction separately for shock upstream and downstream flow-fields and retain terms up to second-order in fluctuations, i.e.

$$\frac{\partial v'_1}{\partial t} + \bar{U}_1 \frac{\partial v'_1}{\partial x} + \frac{1}{\bar{\rho}_1 + \rho'_1} \frac{\partial(\bar{P}_1 + p'_1)}{\partial y} + (u'_1 - \xi_t) \frac{\partial v'_1}{\partial x} + v'_1 \frac{\partial v'_1}{\partial y} = 0, \tag{3.5a}$$

$$\frac{\partial v'_2}{\partial t} + \bar{U}_2 \frac{\partial v'_2}{\partial x} + \frac{1}{\bar{\rho}_2 + \rho'_2} \frac{\partial(\bar{P}_2 + p'_2)}{\partial y} + (u'_2 - \xi_t) \frac{\partial v'_2}{\partial x} + v'_2 \frac{\partial v'_2}{\partial y} = 0. \tag{3.5b}$$

These two equations can be combined and rearranged to get an expression for the shock-downstream velocity gradient as

$$\begin{aligned} \bar{U}_2 \frac{\partial v'_2}{\partial x} &= \xi_{yt} \Delta \bar{U} + \frac{1}{\bar{\rho}_1} \frac{\partial p'_1}{\partial y} - \frac{1}{\bar{\rho}_2} \frac{\partial p'_2}{\partial y} + \bar{U}_1 \frac{\partial v'_1}{\partial x} - \frac{\rho'_1}{\bar{\rho}_1^2} \frac{\partial p'_1}{\partial y} + \frac{\rho'_2}{\bar{\rho}_2^2} \frac{\partial p'_2}{\partial y} + (u'_1 - \xi_t) \frac{\partial v'_1}{\partial x} \\ &- (u'_2 - \xi_t) \frac{\partial v'_2}{\partial x} + v'_1 \frac{\partial v'_1}{\partial y} - v'_2 \frac{\partial v'_2}{\partial y}, \end{aligned} \tag{3.6}$$

where $\Delta \bar{U} = (\bar{U}_2 - \bar{U}_1)$ and the momentum conservation equation in the shock-transverse direction is used to replace time derivatives of velocity in terms of ξ_{yt} .

We now combine (3.4) and (3.6) to write the shock-downstream vorticity fluctuations, and collect the first and second-order terms in $\Omega^{(1)}$ and $\Omega^{(2)}$, respectively. Because the vorticity wave upstream of the shock does not produce any density or pressure fluctuations, these are set to zero. We have

$$\Omega_2^{(1)} = r \frac{\partial v'_1}{\partial x} - \frac{\partial u'_1}{\partial y} + \xi_{yt} (1 - r) + \frac{1}{\bar{\rho}_1 \bar{U}_2} \frac{\partial p'_1}{\partial y} - \frac{1}{\bar{\rho}_2 \bar{U}_2} \frac{\partial p'_2}{\partial y} - \frac{\partial}{\partial y} \left[\frac{p'_1 - p'_2}{2\bar{\rho}_1 \bar{U}_1} - \frac{\bar{U}_2 \rho'_2}{2\bar{\rho}_2} \right], \tag{3.7a}$$

$$\begin{aligned} \Omega_2^{(2)} &= \frac{(u'_1 - \xi_t)}{\bar{U}_2} \frac{\partial v'_1}{\partial x} - \frac{(u'_2 - \xi_t)}{\bar{U}_2} \frac{\partial v'_2}{\partial x} - \frac{\partial}{\partial y} \left[\frac{(u'_1 - \xi_t)^2}{2\bar{U}_1} - \frac{(u'_2 - \xi_t)^2}{2\bar{U}_2} \right] + \frac{v'_1}{\bar{U}_2} \frac{\partial v'_1}{\partial y} \\ &- \frac{v'_2}{\bar{U}_2} \frac{\partial v'_2}{\partial y} - \frac{\partial \xi_y (v'_2 - v'_1)}{\partial y} + \frac{\partial}{\partial y} \frac{\rho'_2 (u'_2 - \xi_t)}{\bar{\rho}_2} + \frac{\rho'_2}{\bar{U}_2 \bar{\rho}_2^2} \frac{\partial p'_2}{\partial y}. \end{aligned} \tag{3.7b}$$

The first-order vorticity $\Omega_2^{(1)}$ obtained from (3.7a) is analogous to the post-shock vorticity obtained from LIA, and figure 6 shows a match between the current form and that presented by Sinha (2012). However, $\Omega_2^{(2)}$ includes the second-order nonlinear effects in

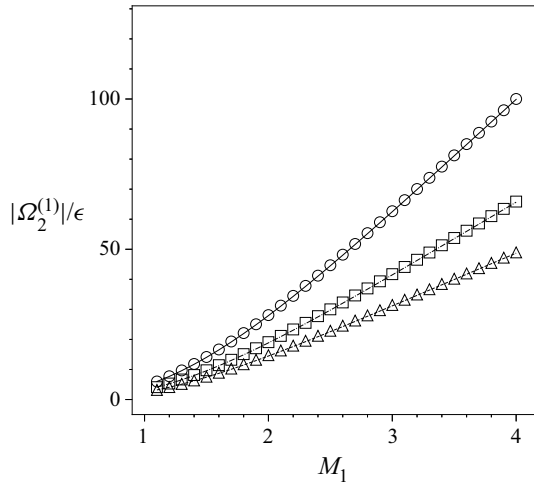


Figure 6. Comparison of the first-order, shock-downstream vorticity fluctuations magnitude $|\Omega_2^{(1)}|$ normalized by the amplitude of upstream vorticity wave ϵ , as obtained from weakly nonlinear framework (line) and LIA (symbol) for $\alpha = 20^\circ$ (circle/solid line), $\alpha = 30^\circ$ (square/dash-dotted line) and $\alpha = 40^\circ$ (triangle/dashed line).

shock-downstream vorticity fluctuations. The last two terms in (3.7b) represent the effects of mass flux and baroclinic generation of vorticity. These terms represent the effect of thermodynamic fluctuations downstream of the shock and their contribution is found to be negligible. This is because of the relatively small magnitude of the shock downstream entropy mode (see figure 2).

After omitting these terms, (3.7b) can be rearranged in the following form to identify the dominant physical mechanisms responsible for higher-order vorticity fluctuations downstream of the shock,

$$\Omega_2^{(2)} \approx \underbrace{\frac{(u'_1 - \xi_t)\Omega'_1 - (u'_2 - \xi_t)\Omega'_2}{\bar{U}_2}}_{\Omega_a} \underbrace{[r(v'_1 + \bar{U}_1\xi_y) - (-\cot\alpha u'_2 + \bar{U}_2\xi_y)]\xi_{yy}}_{\Omega_b} + (r-1) \underbrace{\left[\frac{\partial}{\partial y} \frac{(u'_1 - \xi_t)^2}{2\bar{U}_1} - \xi_y \frac{\partial v'_1}{\partial y} - c_d \cot\alpha (u'_1 - u'_2)\xi_{yy} \right]}_{\Omega_c}, \quad (3.8)$$

where $c_d = (r+1)/(r-1)$. A detailed derivation of this equation is given in Appendix A.

The first group of terms, denoted by Ω_a , represent the turbulent transport of vorticity fluctuations across the unsteady shock wave. The process is driven by the streamwise velocity fluctuations in the shock frame of reference $(u' - \xi_t)$ and the net convective flux of vorticity fluctuations across the shock wave is encapsulated in Ω_a .

The second group of terms denoted by Ω_b is a product of the shock-transverse velocity fluctuations $v' + \bar{U}\xi_y$ with the curvature ξ_{yy} of the deformed shock wave. A curved shock is known to generate vorticity via Crocco's theorem and it appears as a second-order effect in shock-vorticity wave interaction. The curvature effect in Ω_b is also similar to the vorticity produced owing to the curvature of a tangential stress-free surface (Longuet-Higgins 1992, 1998).

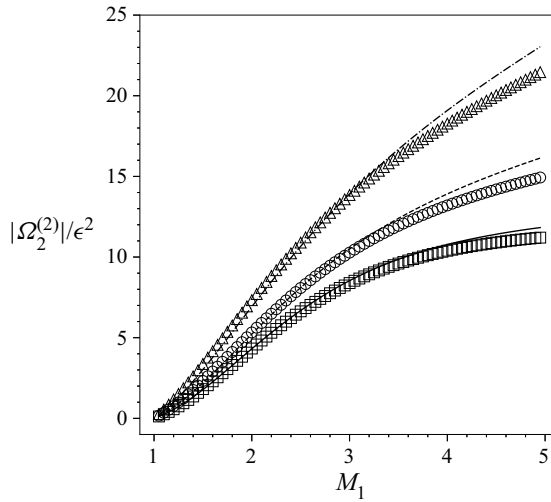


Figure 7. Variation of normalized $\Omega_2^{(2)}$ from (3.8) (symbol) and $\Omega_a + \Omega_b$ (line) at $\alpha = 20^\circ$ (square/solid line), $\alpha = 30^\circ$ (circle/dashed line) and $\alpha = 40^\circ$ (triangle/dash-dotted line).

The remaining terms are grouped together as Ω_c and it is proportional to the factor $r - 1$. Note that r is the density ratio across the shock wave and is close to unity for weak shock waves; hence, the contribution of Ω_c is expected to be small for such cases. Figure 7 compares the amplitude of $\Omega_2^{(2)}$ in (3.8) and the amplitude of $\Omega_a + \Omega_b$ for $\alpha = 20^\circ, 30^\circ$ and 40° . Second-order vorticity amplitude increases with M_1 and reaches an asymptotic limit (not shown). The plot shows Ω_c has negligible contribution to second-order vorticity below $M_1 \approx 3$. In other words, second-order contributions to shock-downstream vorticity fluctuations for lower α and M_1 arise primarily from the shock curvature and turbulent flux of vorticity across the shock.

It is easy to check that the second-order vorticity $\Omega^{(2)}$ given by (3.8) is proportional to ϵ^2 , as terms such as u', Ω', ξ_l are proportional to ϵ (see § 2.1). We therefore divide $\Omega^{(2)}$ by ϵ^2 and further normalize it by $k\bar{U}_1$ to get a non-dimensional parameter ϕ that characterizes the second-order shock-downstream vorticity fluctuations,

$$\phi(M_1, \alpha) = \frac{|\Omega_2^{(2)}|}{\epsilon^2 \bar{U}_1 k} \approx \frac{|\Omega_a| + |\Omega_b|}{\epsilon^2 \bar{U}_1 k}. \tag{3.9}$$

Here, $|\cdot|$ represents complex amplitude. The complex amplitudes of Ω_a and Ω_b can be written in terms of the LIA transfer coefficients of vorticity Z_{vv} , pressure Z_{vp} and shock deformation Z_{vx} ,

$$\begin{aligned} \frac{|\Omega_a|}{\epsilon^2 \bar{U}_1 k} &= -r \sin \alpha + \sin \alpha \frac{Z_{vv}^2}{r} + \sin \alpha \left(\frac{\cos \alpha^p Z_{vv} Z_{vp}}{r \sin \alpha^s \gamma M_2 \zeta} \right) \\ &\quad - i Z_{vx} \cos \alpha \left(r - \frac{Z_{vv} \sin \alpha}{\sin \alpha^s} \right), \end{aligned} \tag{3.10}$$

Weakly nonlinear framework

$$\frac{|\Omega_b|}{\epsilon^2 \bar{U}_1 k} = \sin^2 \alpha \, iZ_{vx} \left\{ r(-\cos \alpha + \sin \alpha \, iZ_{vx}) - \frac{1}{r} \left[-\cot \alpha \left(\sin \alpha^s Z_{vv} + \frac{\cos \alpha^p Z_{vp}}{\gamma M_2 \zeta} \right) + \sin \alpha \, iZ_{vx} \right] \right\}. \quad (3.11)$$

In (3.10), the first term corresponds to the upstream contribution to the turbulent transport of vorticity (Ω_a), while the downstream contribution to Ω_a can be written as

$$(u'_2 - \xi_t) \Omega'_2 = u'^{\Omega}_2 \Omega'_2 + u'^p_2 \Omega'_2 - \xi_t \Omega'_2, \quad (3.12)$$

where the velocity fluctuation is split into its vortical (u'^{Ω}_2) and acoustic (u'^p_2) components. The vortical part is given by the Z^2_{vv}/r term in (3.10). However, the $Z_{vv}Z_{vp}$ term in (3.10) corresponds to the transport of shock-downstream vorticity owing to the velocity fluctuations in the acoustic waves generated by the shock. This represents an inter-modal interaction between the post-shock vorticity and acoustic components to generate second-order vorticity fluctuations.

4. Validation of weakly nonlinear framework

We present results from LIA and inviscid numerical simulations (henceforth denoted as N) for shock-upstream Mach numbers, $M_1 = \{1.25, 1.5, 1.75, 2\}$ at vorticity wave inclinations, $\alpha = \{20^\circ, 30^\circ, 40^\circ\}$. Higher values of M_1 and α increase the numerical error, while the deviation from LIA is too low for lower values. We choose this range as numerical simulations are performed for a fixed value of shock parallel wavenumber $k_y = 2$. The incidence angles chosen are also in the propagating regime of downstream acoustic waves.

Figure 8 shows the comparison of the y -component of instantaneous vorticity profiles immediately downstream of the shock for $\epsilon = 0.01$ and 0.2 at $M_1 = 1.5$ and $\alpha = 25^\circ$. The vorticity profiles are normalized with the amplitude of shock-downstream vorticity ($|\Omega_2^{(1)}|$) computed from (3.7a). Normal shock amplifies the vorticity owing to compression, and the amplification across the shock is a function of the upstream wave for a given α and M_1 . Moreover, the wavelength of the vorticity wave decreases across the shock and it depends on the incidence angle α . LIA predicts sinusoidal patterns for downstream vorticity waves, and the vorticity profiles from the LIA and numerical simulations show excellent agreement for $\epsilon = 0.01$. However, as we increase ϵ to 0.2 , vorticity profiles from numerical simulations deviate from LIA. Nonlinear effects arising from modal interactions become dominant at higher ϵ , as expected.

Figure 9 shows a similar comparison of LIA and numerical simulations at $M_1 = 1.25$ and 1.75 for $\epsilon = 0.2$ and $\alpha = 25^\circ$. Vorticity profiles from LIA and numerical simulations show only a small deviation at $M_1 = 1.25$, whereas the difference grows at $M_1 = 1.75$. This implies that the effect of nonlinear interactions at a given ϵ increases with M_1 . Our goal is to study these nonlinear effects using the weakly nonlinear framework presented in the previous section for various values of shock upstream vorticity amplitude (ϵ), Mach number (M_1) and vorticity wave incidence angle (α).

A measure of the deviation of LIA from numerical simulations is obtained using the idea of root-mean-square (r.m.s.) error σ_N , which is calculated at a position (x) just downstream

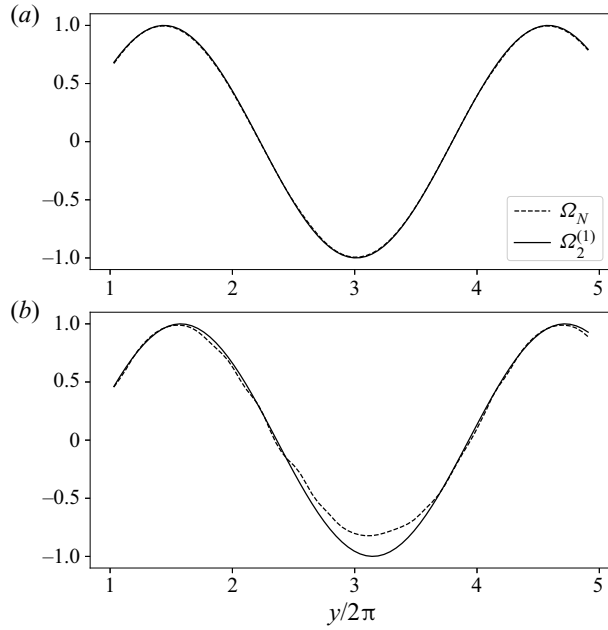


Figure 8. Variation of y -component of vorticity from LIA (solid line) and numerical simulations (dashed line) immediately downstream of the shock for (a) $\epsilon = 0.01$; (b) $\epsilon = 0.2$, for $\alpha = 25^\circ$ and $M_1 = 1.5$. Here, Ω'_2 is normalized with the amplitude of $\Omega_2^{(1)}$.

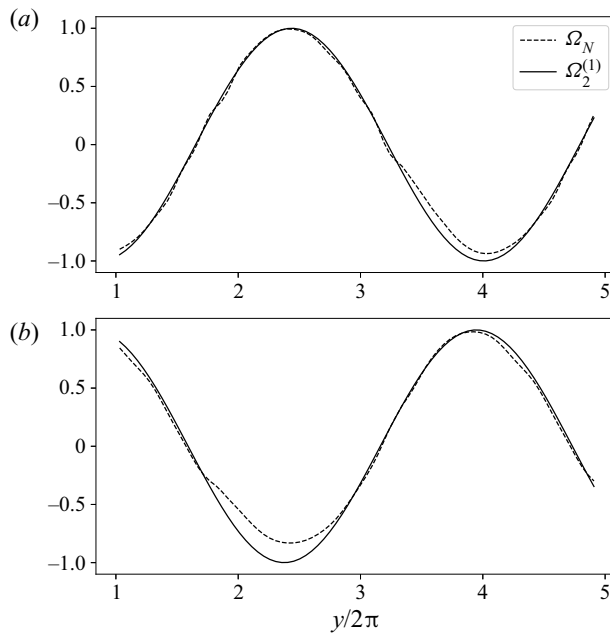


Figure 9. Variation of y -component of vorticity from LIA (solid line) and numerical simulations (dashed line) immediately downstream of the shock for (a) $M_1 = 1.25$; (b) $M_1 = 1.75$, for $\epsilon = 0.2$, $\alpha = 25^\circ$. Here, Ω'_2 is normalized with the amplitude of $\Omega_2^{(1)}$.

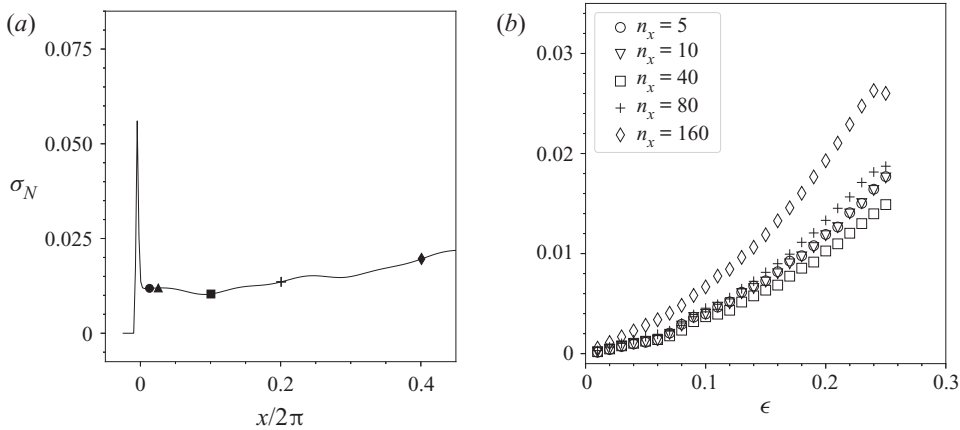


Figure 10. Variation of σ_N for $\alpha = 25^\circ$ and $M_1 = 1.5$ (a) at various x locations downstream of the shock for $\epsilon = 0.2$, (b) with ϵ at various x locations: $n_x = 5$ ($x \approx 0.075$, circle); $n_x = 10$ ($x \approx 0.15$, triangle); $n_x = 40$ ($x \approx 0.625$, square); $n_x = 80$ ($x \approx 1.25$, +); $n_x = 160$ ($x \approx 2.5$, diamond).

of the shock as

$$\sigma_N = \frac{1}{\bar{U}_1 k} \sqrt{\frac{1}{N_y N_t} \sum_{m=1}^{N_t} \sum_{n=1}^{N_y} (\Omega_N - \Omega_2^{(1)})^2}, \tag{4.1}$$

where Ω_N represents the fluctuations in vorticity obtained from numerical simulations; it includes both linear and nonlinear effects. The difference $\Omega_N - \Omega_2^{(1)}$ thus represents the contribution of nonlinear effects. Here, N_y is the number of grid points in y direction and N_t is the number of time instants used for calculating σ_N .

Figure 10(a) shows the variation of σ_N with respect to x , downstream of the shock for $\epsilon = 0.2$, $M_1 = 1.5$ and $\alpha = 25^\circ$. The shock lies at $x = 0$, and we observe a sudden spike in σ_N at that location. This is because, mathematically, the shock is a discontinuity in LIA with zero thickness, whereas the numerically captured shock spreads over multiple grid points. Calculation of σ_N inside this finite shock thickness leads to a large error, which is difficult to formalize using the present analysis. We ensure that the point used for the calculation of σ_N does not lie in this region.

We evaluate the variation of σ_N at the locations indicated by black markers in figure 10(a) for various ϵ (see figure 10b). The value of σ_N immediately downstream of the shock is relatively constant over 10–20 grid points before deviating considerably. The data show the sensitivity of σ_N to the x location where it is evaluated. We choose $x = 0.075$ ($n_x = 5$) as the location downstream of the shock, where σ_N is evaluated in this study.

The location for the evaluation of σ_N is chosen considering its potential use in analysing shock–turbulence interaction, where the near-field is dominated by the inviscid acoustic adjustment. It is characterised by non-monotonic variation of the Reynolds stresses and is predicted well by LIA (at least for low turbulence intensities; see the work of Ryu & Livescu 2014). The location of the peak turbulent kinetic energy is often used in literature (Chen & Donzis (2019), Larsson *et al.* (2013), etc.) to study the amplification of turbulence by the shock wave. Viscous dissipation effects are found to be important downstream of the peak turbulent kinetic energy (*TKE*) location. We, therefore, restrict our analysis to the region immediately downstream of the shock ($n_x = 5$ or 10), so as to capture the effect of the shock directly.

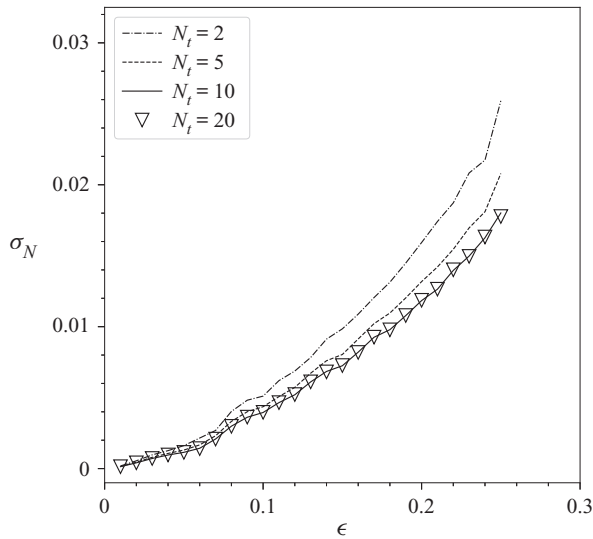


Figure 11. Variation of σ_N with ϵ for $\alpha = 25^\circ$ and $M_1 = 1.5$ for various total time instances (N_t) over one wave period: $N_t = 2$ (dash-dotted line); $N_t = 5$ (dashed line); $N_t = 10$ (solid line) and $N_t = 20$ (triangle).

Effect of variation of the number of time instances (N_t) used in the evaluation σ_N is shown in figure 11. We start with $N_t = 2$ and increase the number of time instances within a wave period. For $N_t = 20$, results are found to be statistically converged.

4.1. Comparison with numerical simulations

Variation of σ_N is shown in figure 12 for $\alpha = \{20^\circ, 30^\circ, 40^\circ\}$, for ϵ ranging from 0.01 to 0.25 and $M_1 = \{1.25, 1.5, 1.75, 2\}$. We notice that σ_N for all the cases considered increases with ϵ and M_1 for a given α . The nonlinear effects are significant at higher ϵ and M_1 owing to the modal interaction at a given α . The results agree with the assertion of the modal interaction made by Chu & Kovásznyai (1958) with a problem involving a shock wave for the first time.

We compare the deviation of the numerical solution from LIA with the second-order effects predicted by the weakly nonlinear framework in figure 13. Note that the nonlinear effects in numerical simulation σ_N are a function of ϵ , M_1 and α . However, ϕ includes the theoretical second-order effects of M_1 and α , while the ϵ^2 variation of $\Omega_2^{(2)}$ is taken out from the definition of ϕ . We plot the ratio σ_N/ϕ to study the effect of M_1 and α on the higher-order vorticity generated by the shock wave. Figure 13 shows that the Mach number variation of σ_N is collapsed by the ratio σ_N/ϕ and the data show a clear trend of ϵ^2 variation at higher ϵ values. There is a systematic deviation towards ϵ scaling in the low amplitude range and it is discussed subsequently. The ϵ^2 scaling is a direct prediction of weakly nonlinear framework and the numerical data support this finding. Moreover, the collapse of the data (for each α) shows that the Mach number scaling predicted by the theory also holds for the numerical solutions. The same is true for the α scaling shown in figure 14. The deviation of the numerical solution from LIA results collapse to a single curve when scaled by the second-order vorticity magnitude obtained from the weakly nonlinear framework. This collapse proves the validity of the weakly nonlinear framework.

Weakly nonlinear framework

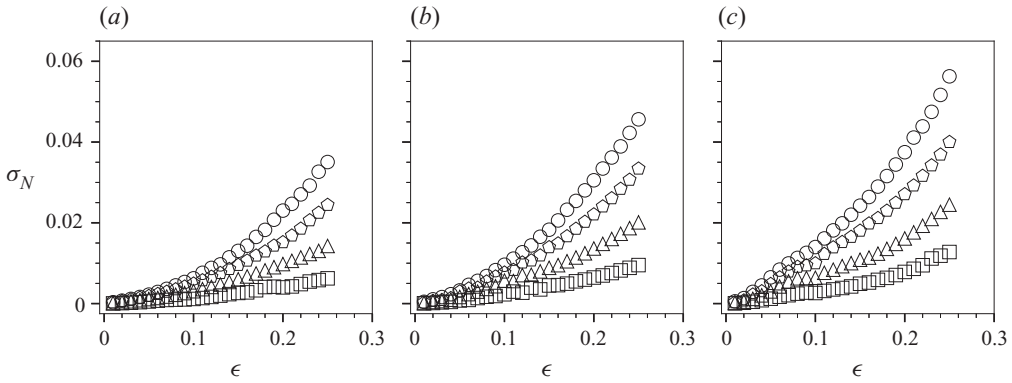


Figure 12. Variation of σ_N with ϵ at $M_1 = 1.25$ (square), $M_1 = 1.5$ (triangle), $M_1 = 1.75$ (pentagon) and $M_1 = 2$ (circle) for: (a) $\alpha = 20^\circ$; (b) $\alpha = 30^\circ$ and (c) $\alpha = 40^\circ$.

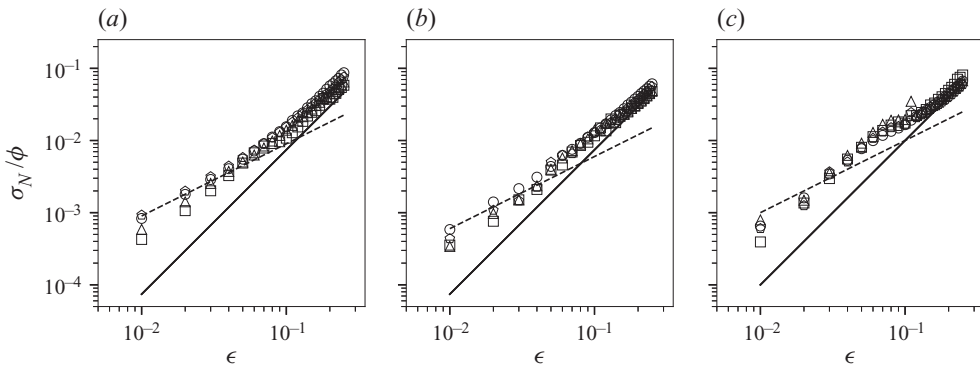


Figure 13. Comparison of WNLF predictions and numerical simulations results. Variation of σ_N/ϕ for $M_1 = 1.25$ (square), $M_1 = 1.5$ (triangle), $M_1 = 1.75$ (pentagon) and $M_1 = 2$ (circle) for: (a) $\alpha = 20^\circ$; (b) $\alpha = 30^\circ$ and (c) $\alpha = 40^\circ$. The variation of σ_N with ϵ collapses to a single curve when scaled by the magnitude of ϕ . Lines show the ϵ^2 (solid) and ϵ (dashed) variation.

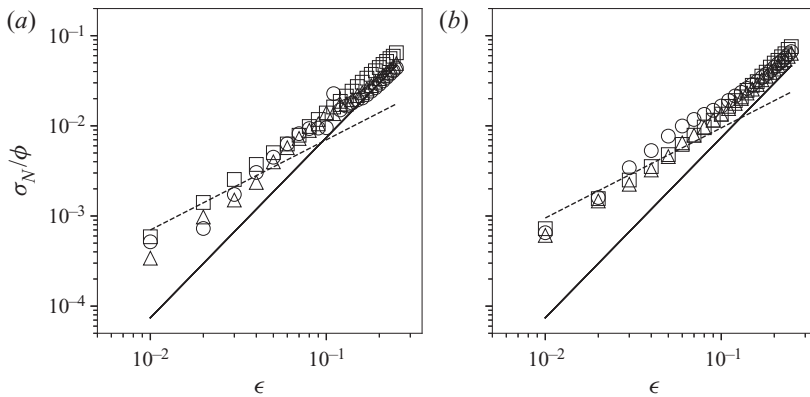


Figure 14. Collapse of the numerical data with respect to incidence angle: the ratio σ_N/ϕ for different α (20° square, 30° triangle and 40° circle) plotted against ϵ for different Mach numbers. Lines show the ϵ^2 (solid) and ϵ (dashed) variation with (a) $M_1 = 1.5$ and (b) $M_1 = 2$.

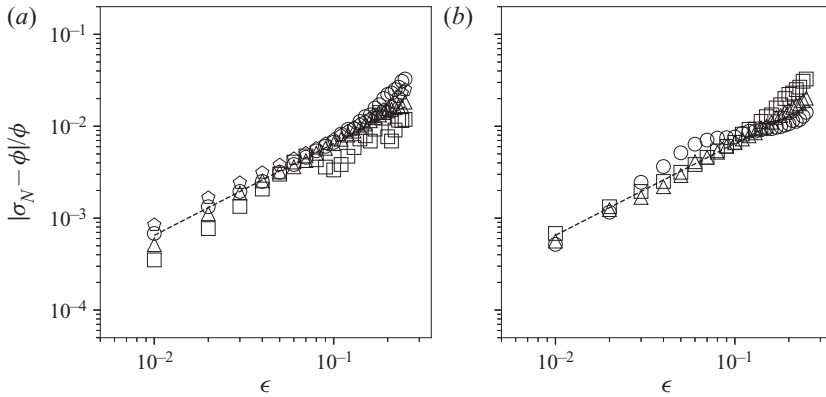


Figure 15. The absolute error $|\sigma_N - \phi|$ scaled by ϕ plotted as a function of ϵ (a) for varying M_1 (1.25, square; 1.5, triangle; 1.75, pentagon and 2.0, circle) for $\alpha = 20^\circ$ and (b) for varying α (20° , square; 30° , triangle and 40° , circle) at $M_1 = 2$. Line represents the ϵ variation.

Figure 15 plots the difference between σ_N and ϕ at various M_1 and α ; the data are once again scaled by ϕ . It is observed that the difference is in the range 10^{-2} to 10^{-4} and approximately varies linearly with ϵ . Although the difference is small in magnitude compared with the data presented in figures 13 and 14, it is important to investigate the reasons behind this discrepancy.

The discrepancies between σ_N and ϕ are possibly related to the numerical challenges faced in the computations and the procedure used to evaluate σ_N . The error related to numerical techniques are discussed by Johnsen *et al.* (2010) and have been minimized while carrying out this study. The selection of the x location used to calculate σ_N downstream of the shock and the phase difference between theoretical and numerical waves upstream of the shock contributes to some error. We ensure that we minimize these errors and it is found to be of the order of 10^{-5} or smaller.

Finally, and perhaps more significantly, the numerical simulations capture the unsteady oscillating shock wave on a Cartesian computational grid. This introduces errors in shock capturing owing to misalignment between the shock shape and the grid lines (Ching *et al.* 2019; Kitamura 2013), and creates discrete jumps in the shock profile, as shown in figure 16. Note that the figure is highly magnified in the vicinity of the shock wave, such that the shock profile over two grid cells is clearly visible in terms of the pressure contours. The magnification in the x -direction exceeds that in the y -direction by a factor of 5. Each jump introduces an additional curvature to the numerically captured shock wave, and it generates non-physical vorticity, entropy and related quantities behind the shock. It is observed that the number of jumps in the shock wave increases proportionately with the amplitude of the shock motion (compare figures 16(a) and 16(b)). The shock amplitude, in turn, is proportional to the amplitude of the incoming vorticity wave (ϵ), as per the assumption in linear theory. The shock-grid misalignment error can therefore be expected to scale linearly with ϵ , denoted by the dashed lines in figure 15.

Note that the sinusoidal deformation of the shock wave is an inherent feature of the shock–vorticity wave interaction. It cannot be neglected even at low values of ϵ . The shock-capturing error is therefore small, but finite at low ϵ . As we increase the amplitude of the upstream vorticity wave, higher-order effects become important and the scaling shifts from $O(\epsilon)$ to $O(\epsilon^2)$ (see figures 13 and 14). After removing the $O(\epsilon)$ error shown in figure 15, the variation of the corrected σ_N/ϕ is plotted in figures 17 and 18. We find

Weakly nonlinear framework

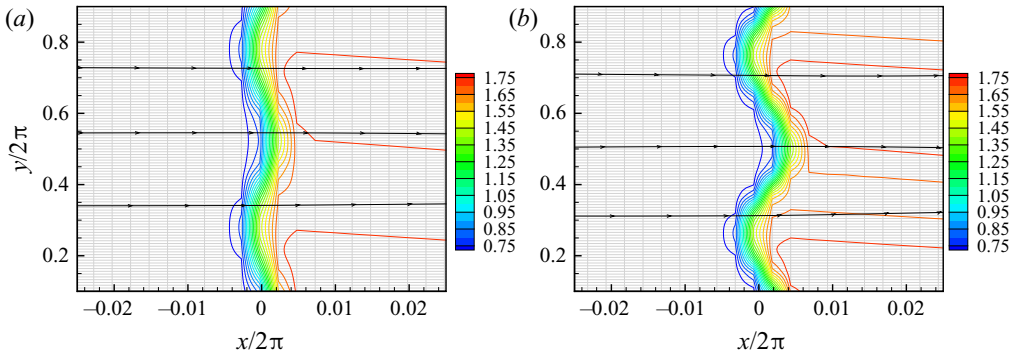


Figure 16. Pressure contours show corrugations in the numerically captured shock wave on a Cartesian grid leading to shock–grid misalignment error for $\alpha = 25^\circ$ and $M_1 = 1.5$: (a) $\epsilon = 0.1\%$; (b) $\epsilon = 0.2\%$.

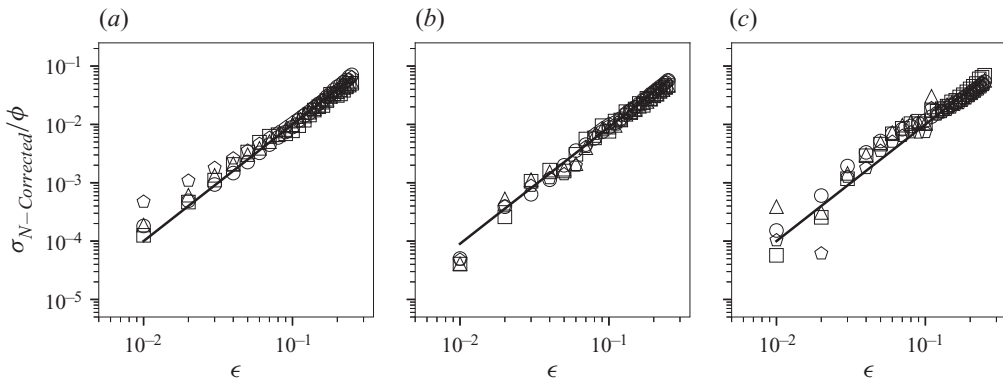


Figure 17. Collapse with respect to M_1 : the ratio σ_N/ϕ after removing $O(\epsilon)$ error for different α (20° , square; 30° , triangle and 40° , circle) plotted against ϵ for different Mach number. Line shows the ϵ^2 variation.

that the scaled variation now varies clearly as $O(\epsilon^2)$ over the entire range of parameters considered in this work.

The magnitude of ϕ constitutes the nonlinear effects in vorticity as given by (3.8) and follows the trend of σ_N accurately after correcting for numerical error. This means that the physics which governs nonlinear effects in vorticity as a function of M_1 is captured by ϕ in the weakly nonlinear range of $\epsilon \leq 0.25$. These results strongly confirm the usefulness of the weakly nonlinear framework presented in § 3.1, which is correct up to second-order in ϵ .

It is important to study the scaling of these nonlinear effects with respect to M_1 . Existence of scaling allows the predictions of variations at different M_1 without performing numerical simulations for each individual case. The results from LIA can also be improved by offsetting for the error accordingly. Scaling could be valuable for problems of the shock–turbulence interaction, where DNS of the problem at higher M_1 becomes increasingly more difficult to perform.

4.2. Parameter space

The weakly nonlinear framework presented in this work uses the results of LIA to study the nonlinear effects in the shock–vorticity interaction. As per LIA, the shock–downstream

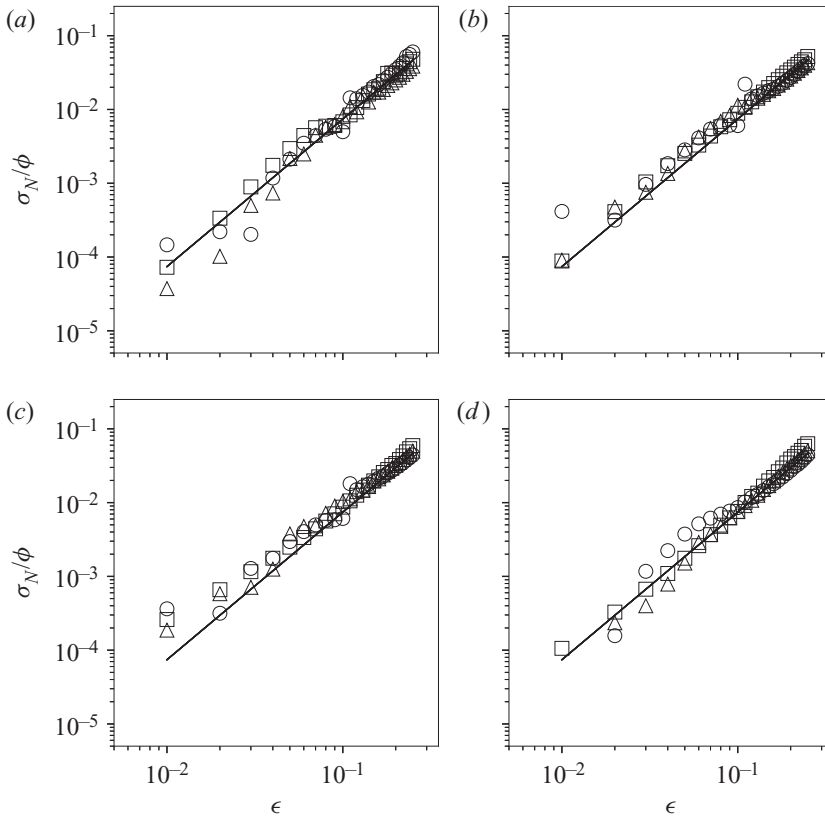


Figure 18. Variation for σ_N scaled by the magnitude of ϕ with ϵ after removing $O(\epsilon)$ error for $\alpha = 20^\circ$ (square), $\alpha = 30^\circ$ (triangle) and $\alpha = 40^\circ$ (circle) for (a) $M_1 = 1.25$, (b) $M_1 = 1.5$, (c) $M_1 = 1.75$, (d) $M_1 = 2$. Solid line shows ϵ^2 variation.

disturbance field is a function of the upstream vorticity wave amplitude ϵ , incidence angle α and the shock strength given by the flow Mach number M_1 . We consider these three parameters for characterizing the nonlinear effects. The results from linear theory also depend on the wavenumber of the upstream wave. Here, we keep the transverse component of the upstream wavenumber constant ($k_y = 2$). Therefore, the upstream wavenumber $k = k_y/\sin \alpha$ changes with the incidence angle.

Nonlinear effects in the shock–disturbance interactions are primarily driven by the intensity of fluctuations (ϵ) upstream of the shock. The separation of linear and nonlinear regimes based on ϵ is not clearly defined for such interactions. Here, we use existing literature on the shock–turbulence interaction to guide the choice of the range of ϵ used to study the nonlinear effects. Canonical shock–turbulence interactions are classified as lying in either a wrinkled regime or a broken shock regime. At low disturbance intensities, the shock front remains intact but has unsteady corrugation. At large values of turbulence intensities, the shock front may disappear locally, giving rise to what are called as shock holes. LIA does not predict shock holes and is therefore valid only in the wrinkled regime. The same is expected to be true for the weakly nonlinear framework that builds upon the LIA solution.

The criteria $M_t/(M_1 - 1) = 0.6$ given by Donzis (2012b) is often used to demarcate the wrinkled and broken-shock regimes, where M_t is the turbulent Mach number that

quantifies the intensity of the upstream turbulent fluctuations. It is related to the vorticity wave amplitude ϵ as $M_t = \epsilon M_1$. We restrict the range of ϵ in our study to meet this criteria for wrinkled shock interaction. For the chosen range of Mach numbers between 1.25 and 2.0, this gives the maximum value of ϵ to be between 0.12 and 0.3. We thus choose ϵ to vary between 0.01 and 0.25 to study the weakly nonlinear effects at the shock wave. As per (3.9), the normalized second-order vorticity $\Omega_2^{(2)}$ is proportional to $\epsilon^2 \phi$, where ϕ is $O(1)$. The deviation of the numerical solution from LIA is therefore expected to have a magnitude $\epsilon^2 \sim 0.06$ as can be observed from figure 12.

The nonlinearity at the shock wave is also driven by inter-modal interaction, as noted in § 3. In the current study, the upstream disturbance field is purely vortical, while the downstream disturbances include vorticity, acoustic and entropy modes. As per the LIA, amplification across the shock is characterized by the transfer coefficients plotted in figure 2. We note the high values of Z_{vv} and Z_{vx} in the vicinity of the critical incidence α_c , which can limit the applicability of LIA and the weakly nonlinear framework. The value of α_c is approximately 62° for the range of Mach numbers considered here, and we restrict the range of α to approximately 60° . The results for $\alpha = 20^\circ\text{--}40^\circ$ are presented in § 4.1, while the higher values of α are discussed in § 5.

We use the weakly nonlinear framework to explore second-order vorticity for Mach numbers up to 5. The LIA transfer coefficients are found to reach close to their asymptotic values in the hypersonic regime. The same is expected to hold for $\Omega_2^{(2)}$. The comparison with numerical solution (§ 4.1) is limited to Mach 2, primarily owing to the limitations of the numerical methodology. The shock-grid misalignment error increases with shock strength, which makes it difficult to perform a meaningful comparison with the theoretical predictions. The same is true for incidence angles α beyond 40° and in the decaying regime ($\alpha > \alpha_c$).

The Mach number range from 1.25 to 2.0 is important in many high-speed flow applications. The Mach number in a scramjet combustor is in this range, where shock-induced mixing is important for efficient combustion. Shock–boundary layer interactions in hypersonic intakes may have a higher Mach number at the boundary layer edge, but the shock waves are highly inclined to the flow. The shock-normal Mach number is much lower, often in the range of 1–2 for a free stream Mach number of 5 (Schulein 2006) and even as high as 13 (Pasha & Sinha 2012). Also, experiments studying the shock–turbulence interaction in wind tunnels are conducted in the low supersonic range because it is difficult and expensive to conduct them at higher M_1 .

5. Predictions of WNLF

We use the weakly nonlinear framework presented in § 3 to derive a limit for the validity of LIA for a range of Mach numbers. The theory is also used to study the nonlinear effects in vorticity at high M_1 and α close to the critical angle (α_c).

5.1. LIA limit

The applicability of LIA is evaluated by comparing the magnitude of the LIA-predicted vorticity ($\Omega_2^{(1)}$) given by (3.7a) and that of the second-order effect ($\Omega_2^{(2)}$) given by WNLF in (3.8). LIA is expected to be valid when

$$\Omega_2^{(2)} \ll \Omega_2^{(1)}. \quad (5.1)$$

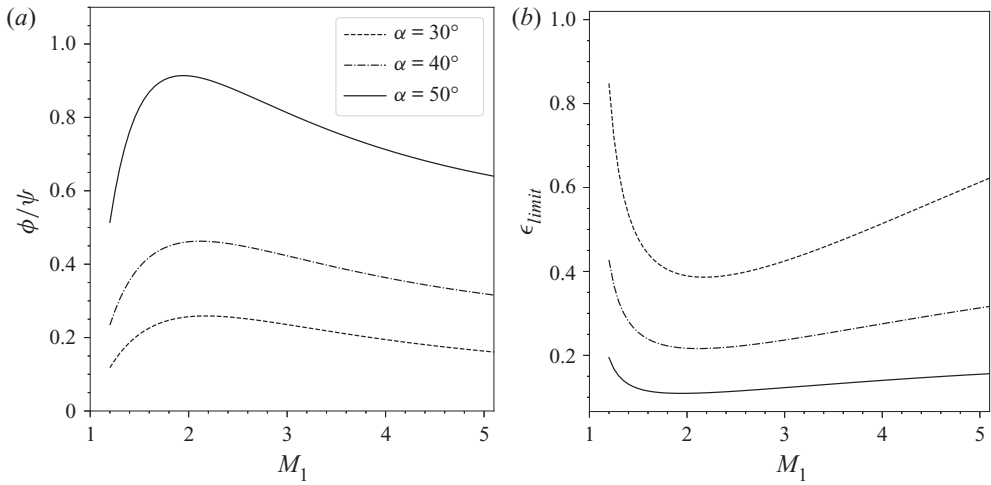


Figure 19. Nonlinear effects in vorticity amplification represented using (a) a relative measure ϕ/ψ , (b) an absolute measure ϵ_{limit} .

We have from (3.9), $\phi = |\Omega_2^{(2)}|/\epsilon^2 \bar{U}_1 k$. Let us define ψ as

$$\psi = \frac{|\Omega_2^{(1)}|}{\epsilon \bar{U}_1 k}. \tag{5.2}$$

We plot the ratio ϕ/ψ as a function of M_1 , for different α , in figure 19(a). As M_1 is increased, for a given α , we observe that the ratio at first increases, reaches a maximum value and then decreases to attain an asymptotic limit in the hypersonic range. This can be understood in terms of the variation of the linear and second-order vorticity with Mach number, as discussed below.

The ratio ϕ/ψ approaches zero in the limit $M_1 \rightarrow 1$, as $\phi \rightarrow 0$ and $\psi \rightarrow 1$. This is because

$$\Omega_2^{(1)} \rightarrow \Omega_1^{(1)} \neq 0 \quad \text{whereas} \quad \Omega_2^{(2)} \rightarrow 0, \tag{5.3}$$

in this limit. In other words, the vorticity amplitude remains unaltered across an infinitely weak shock, which results in a finite value of the downstream linear vorticity. By comparison, the second-order vorticity becomes negligible in magnitude in the sonic limit. This is because $u'_1 = u'_2$, $\Omega'_1 = \Omega'_2$ and $\xi_t = \xi_y = 0$ for a vanishing shock wave. Thus, the contribution of Ω_a in (3.8) drops out and there is no net turbulent transport in the case of an infinitely weak shock wave. The other terms $\Omega_b = \Omega_c = 0$ by virtue of $\xi_{yy} = 0$ and $r = 1$, respectively, which results in a vanishing value of the second-order vorticity in this limit.

Using Taylor series expansion of ϕ and ψ in the vicinity of the sonic point and retaining only the first-order term in Mach number, we can write

$$\frac{\phi}{\psi} = \frac{\phi'(M_1 - 1)}{1 + \psi'(M_1 - 1)} \approx \phi'(M_1 - 1) + O(M_1 - 1)^2, \tag{5.4}$$

where ϕ' and ψ' represent the derivative with respect to Mach number of the corresponding function. The slope of the ratio ϕ/ψ in figure 19(a) is therefore determined by the derivative ϕ' . For weak shocks, the second-order vorticity increases in magnitude

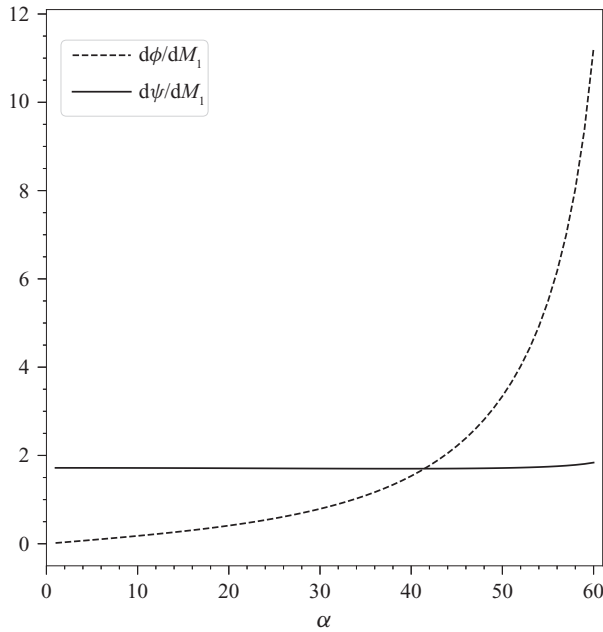


Figure 20. The slope of ϕ and ψ in the limit of $M_1 \rightarrow 1$ as a function of incidence angle α .

with increasing Mach number (see figure 7). Thus, the derivative ϕ' is positive, and it increases with α in the propagating regime. However, the initial slope of ψ at $M_1 = 1$ is independent of Mach number, as

$$\psi = Z_{vv} \propto r, \tag{5.5}$$

and

$$\lim_{M_1 \rightarrow 1} \frac{d\psi}{dM_1} = \lim_{M_1 \rightarrow 1} \frac{dr}{dM_1} = \frac{4}{\gamma + 1}. \tag{5.6}$$

The limiting slopes ϕ' and ψ' are plotted as a function of α in figure 20. Together, they give an increasing trend for the ratio ϕ/ψ for Mach numbers close to 1. However, although both $\Omega_2^{(2)}$ and $\Omega_2^{(1)}$ reach asymptotic values in the large M_1 limit, the growth of $\Omega_2^{(2)}$ becomes smaller as M_1 increases and reaches an asymptotic limit for smaller M_1 when compared with $\Omega_2^{(1)}$ (see figures 6 and 7 which plot ϕ and ψ). This results in a decreasing trend for ϕ/ψ for Mach numbers beyond 2, as is observed in figure 19(a). In the large M_1 limit, this ratio reaches an asymptotic value that depends only on α . Thus, we get a local peak in ϕ/ψ , which corresponds to the Mach number, where the second-order effects are the largest compared with the first-order vorticity amplification, once the amplitude factors are scaled out.

The ratio ϕ/ψ is also observed to increase with the incidence angle α (not shown). This behaviour in the low-Mach-number regime is in line with the results presented in figure 12 of § 4, whereas the variation for large Mach numbers is predicted using the weakly nonlinear framework presented in § 3. In short, the LIA prediction of vorticity amplification increases with α , as per the variation of Z_{vv} shown in figure 2(a).

In comparison, $\Omega_2^{(2)}$ varies as the product of two transfer coefficients, such as $Z_{vv}Z_{vp}$ or $Z_{vv}Z_{vv}$ (as per (3.7b)) resulting in the observed trend in figure 2(a).

Next, we rewrite (5.1) in terms of the functions ϕ and ψ to arrive at a limit on ϵ for LIA to be valid,

$$\epsilon_{limit} = 0.1 \frac{\psi}{\phi}. \tag{5.7}$$

Here, a factor of 0.1 is introduced to change the inequality to equality under the assumption that the second-order vorticity is less than or equal to 10% of the linear vorticity in magnitude. This corresponds to a maximum of 10% error in LIA results.

Figure 19(b) shows the variation of ϵ_{limit} with M_1 for various α values evaluated using (5.7). As expected, the variation of ϵ_{limit} with M_1 at a given α is non-monotonic. It decreases with increasing M_1 for weak shocks, reaches a local minima and subsequently increases for higher Mach numbers. It is opposite to the trend observed in figure 19(a), where the ratio ϕ/ψ gives the relative measure of nonlinearity in vorticity. However, figure 19(b) provides an absolute quantitative limit on the upstream vorticity wave amplitude as a function of flow parameters. At a given α and M_1 , ϵ values above ϵ_{limit} would breach the limit of LIA validity, which results in the prediction that have more than 10% error.

The minimum value of ϵ_{limit} is attained at $M_1 \simeq 2$ for the different α values shown in figure 19(b). This poses the strictest limit on the range of upstream vorticity magnitude ϵ for which LIA results are accurate. At lower Mach numbers ($M_1 < 2$), higher values of ϵ are permissible. In fact, the ϵ_{limit} curves have a singular behaviour at $M_1 = 1$. This can be resolved by noting the limiting behaviour of the first-order vorticity and the second-order vorticity given in (5.3).

As noted above, ϵ_{limit} increases with Mach number for $M_1 > 2$, which implies that LIA is valid for a larger range of ϵ at higher Mach numbers, or equivalently, for stronger shock waves. The mean compression of the shock amplifies vorticity disturbances in the flow and this linear effect is accurately predicted by LIA. A stronger shock leads to a higher amplification of vorticity amplitude. However, the second-order vorticity is generated by nonlinear effects owing to the inter-modal interaction and shock-curvature effects, as per the weakly nonlinear framework. The amplitude of the downstream Kovásznyai modes and the shock oscillation both depend on the disturbance level upstream of the shock. The ϵ_{limit} in figure 19(b) can thus be interpreted as a balance between two competing effects. A stronger shock favours the linear effect owing to the mean compression of the shock, while larger amplitude disturbance (higher ϵ) increases the nonlinear contribution. For a given Mach number, the value of ϵ_{limit} is a function of the vorticity wave incidence angle. For the different values of α presented in figure 19(b), ϵ_{limit} increases monotonically at higher Mach numbers, which indicates that LIA has a higher range of validity for strong shock waves.

The validity of LIA for the shock–turbulence interaction is usually prescribed in terms of M_t and M_1 . For example, the criteria $M_t/(M_1 - 1) = 0.6$ is frequently used to demarcate the wrinkled regime and broken shock interactions (Donzis 2012b). The ϵ_{limit} presented above can be interpreted in a similar vein by noting that $\epsilon = M_t/M_1$, such that the values plotted in figure 19(b) give an upper limit on the ratio of M_t to M_1 for the validity of LIA for the shock–vorticity wave interaction. As per the weakly nonlinear framework, this limit is a function of the incidence angle and shock strength. For a given Mach number, (5.7) can be integrated over all possible α (in three-dimensional space) to get an estimate of ϵ_{limit} for the shock–turbulence interaction. Further, the limit is derived based on the magnitude of the second-order vorticity. It may be different if we consider nonlinear

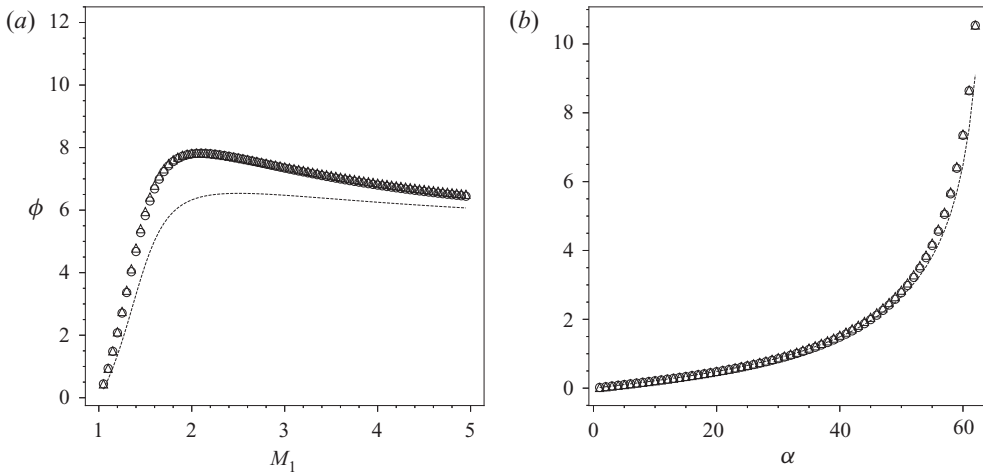


Figure 21. Variation of $\Omega_2^{(2)}$ from (3.8) (circle), $\Omega_a + \Omega_b$ (dashed line) and $\Omega_a + \Omega_b + \Omega_c$ (triangle) with (a) M_1 at $\alpha = 60^\circ$, (b) α at $M_1 = 3$.

effects in other quantities like Reynolds stresses and downstream pressure fluctuations. The weakly nonlinear framework can be extended to study other quantities of interest to get a more general criterion for the validity of LIA.

5.2. Second-order effects at high M_1 and α

We use the expressions derived in § 3 to analyse the nonlinear effects in vorticity amplification for high α and M_1 regime to understand the underlying physics better. Figure 21 shows that the second-order vorticity increases with Mach number (M_1) and reaches an asymptotic value in the hypersonic limit. However, ϕ exhibits a sharp increase near α_c , by approximately a factor of 10 compared with its value at $\alpha = 30^\circ$ considered in § 4.

Figure 22 plots the variation of the constituent terms Ω_a , Ω_b and Ω_c of the second-order vorticity as a function of M_1 and α . At low values of α (see figure 22a), the second-order vorticity is dominated by the turbulent transport term Ω_a and the shock-curvature effect Ω_b . The Ω_c term is comparatively small in magnitude and was neglected in the analysis presented earlier. The Ω_c constitutes the additional effect of the turbulent flux of vorticity and shock-curvature along with dilatation, which becomes significant at α close to α_c . The nonlinear effects at α close to α_c is dominated by Ω_b (see figure 22b). The other parts, Ω_a and Ω_c , have a non-negligible contribution to second-order vorticity at such high α . The dramatic rise in Ω_b for high incidence angles is also visible in figures 22(c) and 22(d), which plot the variation of the constituent terms at $M_1 = 1.75$ and 5, respectively.

The variation of $\Omega_2^{(2)}$ and its constituent terms at high α can be interpreted in terms of the transfer coefficients presented in figure 2(a). Both Z_{vv} and Z_{vx} show a sharp rise in the vicinity of the critical angle and all the transfer coefficients, including Z_{vp} , have singular behaviour at α_c . The resulting intermodal interaction terms in (3.10) and (3.11) also show a similar behaviour, and this would severely restrict the validity of LIA at the critical angle.

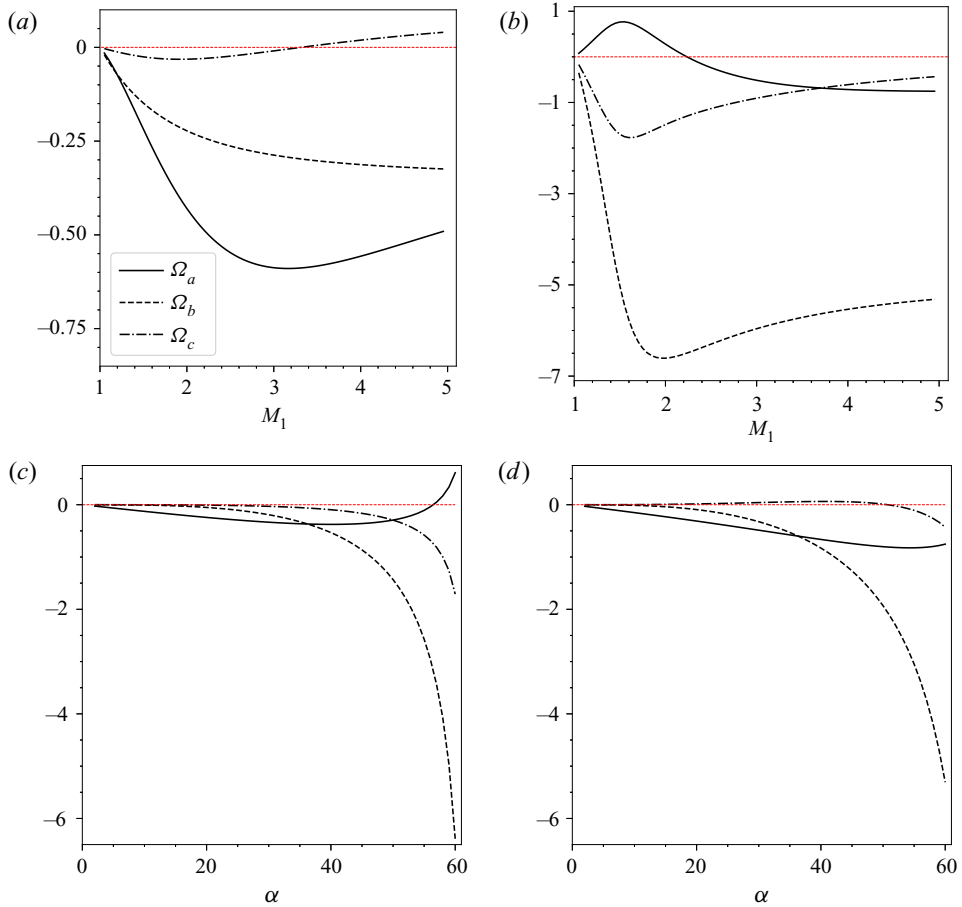


Figure 22. Variation of the magnitude of Ω_a (circle), Ω_b (triangle) and Ω_c (square) from (3.8) with M_1 : (a) at $\alpha = 30^\circ$; (b) at $\alpha = 60^\circ$ and with α (c) at $M_1 = 1.75$; (d) at $M_1 = 5$.

6. Summary and conclusions

In this paper, we present a weakly nonlinear framework for the interaction of two-dimensional vorticity waves with a normal shock. The shock–vorticity interaction is one of the elementary problems that form the basis of linear interaction analysis to study the shock–turbulence interaction. The weakly nonlinear framework presented is based on the inviscid and ideal gas assumptions, where the shock is assumed to be a discontinuity. The nominally normal shock wave distorts and oscillates about its mean position in response to the unsteady fluctuations passing through it. We study second-order effects at the shock wave to identify the physical mechanisms responsible for nonlinear amplification of vorticity across the shock. A range of shock Mach numbers (M_1), vorticity wave amplitudes (ϵ) and incidence angles (α) up to the critical angle are considered.

It is found that the second-order amplification of vorticity increases with the incidence angle of the vorticity wave to reach a singularity at the critical angle. The variation with M_1 is non-monotonic, with a rapid rise at low M_1 to reach an asymptotic value in the hypersonic limit. The analysis predicts that the generation of second-order vorticity at the shock wave is primarily owing to shock curvature and turbulent transport of vorticity. The turbulent transport has a significant contribution from intermodal interaction between the

vorticity and acoustic waves generated at the shock, and it is dominant at low α and low M_1 except close to the sonic limit. However, the shock curvature plays a vital role in vorticity amplification at high α close to the critical value.

We use a high-order accurate numerical method to compute the shock–vorticity interaction for a range of M_1 , ϵ and α . The simulations employ a fifth-order WENO method in the region of the shock wave and a sixth-order central difference scheme in the rest of the domain. The deviation of the numerical solution from LIA prediction, denoted by σ_N , is quantified and compared with predictions of the weakly nonlinear framework. It is found that σ_N has a second-order variation with ϵ and this is in line with the second-order vorticity magnitude obtained analytically. The σ_N value also increases with M_1 and α , matching the trend in the weakly nonlinear framework. Further, the theoretical predictions are able to collapse the numerical data over the range of both Mach number and α tested in the simulations. Thus the weakly nonlinear framework is a valuable addition to LIA that is widely used to study the shock–turbulence interaction.

An important additional contribution of the present framework is to predict a limit to the validity of LIA. We compare the magnitude of vorticity amplification predicted by LIA with the second-order vorticity obtained from the weakly nonlinear analysis. The results are presented in the form of an upper bound to the vorticity wave amplitude, for which the error caused by neglecting higher-order terms is less than 10%. The limiting ϵ value is found to be high for the $M_1 \rightarrow 1$ and $M_1 \rightarrow \infty$ limit, with local minima near $M_1 = 2$ for $\gamma = 1.4$. This implies that LIA is most restrictive at this M_1 , with a higher ϵ range of applicability at higher and lower Mach numbers.

The analysis presented in this work provides a template to study nonlinear effects in more general interactions such as a vortex passing through a shock and the shock–turbulence interaction. The analysis can also be extended to other kinds of upstream disturbances, namely, acoustic waves, entropy waves or their combinations. For a given fundamental mode, its interaction with other modes is governed by the underlying transfer coefficients. For the prediction of nonlinear effects in downstream vorticity in the range studied, we find that the interaction of the vorticity mode with the acoustic mode is most dominant.

The framework exhibited in this paper considers the nonlinear effects arising from the interaction of a pure vorticity wave with a normal shock in an ideal gas. If we consider fluctuations of thermodynamic quantities upstream of the shock, equations need to be adjusted accordingly. This framework is valid specifically in a weakly nonlinear regime where the amplitude of upstream fluctuations is not too large to distort the shock structure significantly. Moreover, the weakly nonlinear framework presented here is valid only at the shock. Further investigation is needed to study the effects of modal interaction downstream of the shock.

Acknowledgements. We thank Prof J. Larsson, University of Maryland, College Park, MD, for providing the code to perform numerical computations presented in this study.

Declaration of interests. The authors report no conflict of interest.

Author ORCIDs.

 Vineeth Nair <https://orcid.org/0000-0002-9921-0352>;

 Krishnendu Sinha <https://orcid.org/0000-0001-7994-2831>.

Appendix A

Higher-order effects in vorticity are given by (3.7b). We derive Ω_a , Ω_b and Ω_c given in (3.8) as follows. We have

$$\begin{aligned} \Omega_2^{(2)} = & \frac{(u'_1 - \xi_t)}{\bar{U}_2} \frac{\partial v'_1}{\partial x} - \frac{(u'_2 - \xi_t)}{\bar{U}_2} \frac{\partial v'_2}{\partial x} - \frac{\partial}{\partial y} \left[\frac{(u'_1 - \xi_t)^2}{2\bar{U}_1} - \frac{(u'_2 - \xi_t)^2}{2\bar{U}_2} \right] + \frac{v'_1}{\bar{U}_2} \frac{\partial v'_1}{\partial y} \\ & - \frac{v'_2}{\bar{U}_2} \frac{\partial v'_2}{\partial y} - \frac{\partial \xi_y (v'_2 - v'_1)}{\partial y} + \frac{\partial}{\partial y} \frac{\rho'_2 (u'_2 - \xi_t)}{\bar{\rho}_2} + \frac{\rho'_2}{\bar{U}_2 \bar{\rho}_2^2} \frac{\partial p'_2}{\partial y}. \end{aligned} \tag{A1}$$

The terms corresponding to shock-unsteadiness, baroclinic torque and the effect of the fluctuations in mass flux are found to be negligible. Therefore, simplifying and rearranging (A1) gives

$$\begin{aligned} \Omega_2^{(2)} \approx & \frac{(u'_1 - \xi_t)\Omega'_1 - (u'_2 - \xi_t)\Omega'_2}{\bar{U}_2} + \frac{v'_1 + \bar{U}_1 \xi_y}{\bar{U}_2} \frac{\partial v'_1}{\partial y} - \frac{v'_2 + \bar{U}_2 \xi_y}{\bar{U}_2} \frac{\partial v'_2}{\partial y} \\ & + \frac{(u'_1 - u'_2)}{\bar{U}_2} \frac{\partial \xi_t}{\partial y} + \frac{b(u'_1 - \xi_t)}{\bar{U}_2} \frac{\partial (u'_1 - \xi_t)}{\partial y} - (v'_2 - v'_1) \xi_{yy} + (1 - r) \xi_y \frac{\partial v'_1}{\partial y}, \end{aligned} \tag{A2}$$

$$\begin{aligned} \approx & \frac{(u'_1 - \xi_t)\Omega'_1 - (u'_2 - \xi_t)\Omega'_2}{\bar{U}_2} + [\cot \alpha (u'_1 - u'_2) + (1 - r)v'_1 + (\bar{U}_2 - r\bar{U}_1)\xi_y] \xi_{yy} \\ & + (r - 1) \left[\frac{\partial}{\partial y} \frac{(u'_1 - \xi_t)^2}{2\bar{U}_1} - \xi_y \frac{\partial v'_1}{\partial y} - \left(\frac{r + 1}{r - 1} \right) \cot \alpha (u'_1 - u'_2) \xi_{yy} \right], \end{aligned} \tag{A3}$$

$$\begin{aligned} \approx & \underbrace{\frac{r(u'_1 - \xi_t)\Omega'_1}{\bar{U}_1} - \frac{(u'_2 - \xi_t)\Omega'_2}{\bar{U}_2}}_{\Omega_a} + \underbrace{[-r(v'_1 + \bar{U}_1 \xi_y) + (-\cot \alpha u'_2 + \bar{U}_2 \xi_y)] \xi_{yy}}_{\Omega_b} \\ & + (r - 1) \underbrace{\left[\frac{\partial}{\partial y} \frac{(u'_1 - \xi_t)^2}{2\bar{U}_1} - \xi_y \frac{\partial v'_1}{\partial y} - c_d \cot \alpha (u'_1 - u'_2) \xi_{yy} \right]}_{\Omega_c}, \end{aligned} \tag{A4}$$

where $c_d = (r + 1)/(r - 1)$. Thus we have for second-order vorticity fluctuations

$$\Omega_2^{(2)} \approx \Omega_a + \Omega_b + \Omega_c. \tag{A5}$$

REFERENCES

ANDREOPOULOS, Y., AGUI, J.H. & BRIASSULIS, G. 2000 Shock wave–turbulence interactions. *Annu. Rev. Fluid Mech.* **32** (1), 309–345.

AUVITY, B., BARRE, S. & BONNET, J.P. 2002 Experimental study of a normal shock/homogeneous turbulence interaction. In *Fluids Engineering Division Summer Meeting*, vol. 36150, pp. 1089–1095. ASME.

BARRE, S., ALEM, D. & BONNET, J.P. 1996 Experimental study of a normal shock/homogeneous turbulence interaction. *AIAA J.* **34** (5), 968–974.

BERMEJO-MORENO, I., BODART, J., LARSSON, J., BARNEY, B.M., NICHOLS, J.W. & JONES, S. 2013 Solving the compressible Navier–Stokes equations on up to 1.97 million cores and 4.1 trillion grid points. In *SC'13: Proceedings of the International Conference on High Performance Computing, Networking, Storage and Analysis*, pp. 1–10. ACM.

BRAUN, N.O., PULLIN, D.I. & MEIRON, D.I. 2019 Large eddy simulation investigation of the canonical shock-turbulence interaction. *J. Fluid Mech.* **858**, 500–535.

- CHANG, C.T. 1957 Interaction of a plane shock and oblique plane disturbances with special reference to entropy waves. *J. Aeronaut. Sci.* **24** (9), 675–682.
- CHEN, C.H. & DONZIS, D.A. 2019 Shock–turbulence interactions at high turbulence intensities. *J. Fluid Mech.* **870**, 813–847.
- CHING, E.J., LV, Y., GNOFFO, P., BARNHARDT, M. & IHME, M. 2019 Shock capturing for discontinuous Galerkin methods with application to predicting heat transfer in hypersonic flows. *J. Comput. Phys.* **376**, 54–75.
- CHU, B.T. & KOVÁSZNAY, L.S.G. 1958 Non-linear interactions in a viscous heat-conducting compressible gas. *J. Fluid Mech.* **3** (5), 494–514.
- DONZIS, D.A. 2012a Amplification factors in shock-turbulence interactions: effect of shock thickness. *Phys. Fluids* **24** (1), 011705.
- DONZIS, D.A. 2012b Shock structure in shock-turbulence interactions. *Phys. Fluids* **24** (12), 126101.
- FABRE, D., JACQUIN, L. & SESTERHENN, J. 2001 Linear interaction of a cylindrical entropy spot with a shock. *Phys. Fluids* **13** (8), 2403–2422.
- FARAG, G., BOIVIN, P. & SAGAUT, P. 2019 Interaction of two-dimensional spots with a heat releasing/absorbing shock wave: linear interaction approximation results. *J. Fluid Mech.* **871**, 865–895.
- GRIFFOND, J. 2005 Linear interaction analysis applied to a mixture of two perfect gases. *Phys. Fluids* **17** (8), 086101.
- GRUBE, N.E. & MARTÍN, M.P. 2021 Reynolds stress anisotropy in shock/isotropic turbulence interactions. *J. Fluid Mech.* **913**, A19.
- HUETE RUIZ DE LIRA, C., VELIKOVICH, A.L. & WOUCHUK, J.G. 2011 Analytical linear theory for the interaction of a planar shock wave with a two- or three-dimensional random isotropic density field. *Phys. Rev. E* **83**, 056320.
- HUETE RUIZ DE LIRA, C., WOUCHUK, J.G. & VELIKOVICH, A.L. 2012 Analytical linear theory for the interaction of a planar shock wave with a two-or three-dimensional random isotropic acoustic wave field. *Phys. Rev. E* **85** (2), 026312.
- JOHNSEN, E., *et al.* 2010 Assessment of high-resolution methods for numerical simulations of compressible turbulence with shock waves. *J. Comput. Phys.* **229** (4), 1213–1237.
- KITAMURA, K. 2013 A further survey of shock capturing methods on hypersonic heating issues. In *21st AIAA Computational Fluid Dynamics Conference*, p. 2698. AIAA.
- KOVÁSZNAY, L.S.G. 1953 Turbulence in supersonic flow. *J. Aeronaut. Sci.* **20** (10), 657–674.
- LARSSON, J., BERMEJO-MORENO, I. & LELE, S.K. 2013 Reynolds-and Mach-number effects in canonical shock-turbulence interaction. *J. Fluid Mech.* **717**, 293–321.
- LARSSON, J. & LELE, S.K. 2009 Direct numerical simulation of canonical shock/turbulence interaction. *Phys. Fluids* **21** (12), 126101.
- LEE, S., LELE, S.K. & MOIN, P. 1993 Direct numerical simulation of isotropic turbulence interacting with a weak shock wave. *J. Fluid Mech.* **251**, 533–562.
- LELE, S.K. & LARSSON, J. 2009 Shock-turbulence interaction: what we know and what we can learn from peta-scale simulations. *J. Phys.: Conf. Ser.* **180**, 012032.
- LIU, J., SHENG, Y. & SISLIAN, J.P. 1995 Shock waves and turbulence in a hypersonic inlet. *Shock Waves* **4** (5), 237–245.
- LIVESCU, D. & RYU, J. 2016 Vorticity dynamics after the shock-turbulence interaction. *Shock Waves* **26** (3), 241–251.
- LONGUET-HIGGINS, M.S. 1992 Capillary rollers and bores. *J. Fluid Mech.* **240**, 659–679.
- LONGUET-HIGGINS, M.S. 1998 Vorticity and curvature at a free surface. *J. Fluid Mech.* **356**, 149–153.
- MAHESH, K., LEE, S., LELE, S.K. & MOIN, P. 1995 The interaction of an isotropic field of acoustic waves with a shock wave. *J. Fluid Mech.* **300**, 383–407.
- MAHESH, K., MOIN, P. & LELE, S.K. 1996 The interaction of a shock wave with a turbulent shear flow. *Tech. Rep.* TF-69. Thermosciences Division, Department of Mechanical Engineering, Stanford University.
- MCKENZIE, J.F. & WESTPHAL, K.O. 1968 Interaction of linear waves with oblique shock waves. *Phys. Fluids* **11** (11), 2350–2362.
- MOORE, F.K. 1954 Unsteady oblique interaction of a shock wave with a plane disturbance. *NACA Tech. Rep.* TR 1165. NACA, supersedes *NACA TN 2879*, 1953.
- PASHA, A.A. & SINHA, K. 2012 Simulation of hypersonic shock/turbulent boundary-layer interactions using shock-unsteadiness model. *J. Propul. Power* **28** (1), 46–60.
- QUADROS, R., SINHA, K. & LARSSON, J. 2016a Kovasznyai mode decomposition of velocity-temperature correlation in canonical shock-turbulence interaction. *Flow Turbul. Combust.* **97** (3), 787–810.
- QUADROS, R., SINHA, K. & LARSSON, J. 2016b Turbulent energy flux generated by shock/homogeneous-turbulence interaction. *J. Fluid Mech.* **796**, 113–157.

- RANJAN, D., OAKLEY, J. & BONAZZA, R. 2011 Shock-bubble interactions. *Annu. Rev. Fluid Mech.* **43** (1), 117–140.
- RIBNER, H.S. 1954 Convection of a pattern of vorticity through a shock wave. *NACA Tech. Rep.* TR 1164. NACA, supersedes *NACA TN 2864*, 1953.
- RIBNER, H.S. 1987 Spectra of noise and amplified turbulence emanating from shock turbulence interaction. *AIAA J.* **25** (3), 436–442.
- ROY, S., PATHAK, U. & SINHA, K. 2018 Variable turbulent Prandtl number model for shock/boundary-layer interaction. *AIAA J.* **56** (1), 342–355.
- RYU, J. & LIVESCU, D. 2014 Turbulence structure behind the shock in canonical shock-vortical turbulence interaction. *J. Fluid Mech.* **756**, R1.
- SCHULEIN, E. 2006 Skin friction and heat flux measurements in shock/boundary layer interaction flows. *AIAA J.* **44** (8), 1732–1742.
- SETHURAMAN, Y.P.M., SINHA, K. & LARSSON, J. 2018 Thermodynamic fluctuations in canonical shock–turbulence interaction: effect of shock strength. *Theor. Comput. Fluid Dyn.* **32** (5), 629–654.
- SINHA, K. 2012 Evolution of enstrophy in shock/homogeneous turbulence interaction. *J. Fluid Mech.* **707**, 74–110.
- SINHA, K., MAHESH, K. & CANDLER, G.V. 2005 Modeling the effect of shock unsteadiness in shock/turbulent boundary-layer interactions. *AIAA J.* **43** (3), 586–594.
- TIAN, Y., JABERI, F.A., LI, Z. & LIVESCU, D. 2017 Numerical study of variable density turbulence interaction with a normal shock wave. *J. Fluid Mech.* **829**, 551–588.
- VEMULA, J.B. & SINHA, K. 2020 Explicit algebraic Reynolds stress model for shock-dominated flows. *Intl J. Heat Fluid Flow* **85**, 108680.
- WOCHUK, J.G., DE LIRA, C.H.R. & VELIKOVICH, A.L. 2009 Analytical linear theory for the interaction of a planar shock wave with an isotropic turbulent vorticity field. *Phys. Rev. E* **79** (6), 066315.
- ZANG, T.A., HUSSAINI, M.Y. & BUSHNELL, D.M. 1984 Numerical computations of turbulence amplification in shock-wave interactions. *AIAA J.* **22** (1), 13–21.